LBL-12269 c.2
Preprint

Lawrence Berkeley Laboratory
UNIVERSITY OF CALIFORNIA

Submitted to Physical Review B

EVIDENCE FROM RELATIVISTIC Ne, Ar, AND Fe DATA FOR "EXCITON-EXCITON" ANNIHILATION AS A NaI:Tl SCINTILLATION SATURATION MECHANISM

M.H. Salamon and S.P. Ahlen

December 1980

Prepared for the U.S. Department of Energy under Contract W-7405-ENG-48

DISCLAIMER

Evidence from Relativistic Ne, Ar, and Fe Data for "Exciton-Exciton" Annihilation as a NaI:Tl Scintillation Saturation Mechanism*

M.H. Salamon and S.P. Ahlen†

Department of Physics
and
Lawrence Berkeley Laboratory
University of California
Berkeley, California 94720

Abstract

Data are presented on the response of NaI:Tl to relativistic ^{20}Ne, ^{40}Ar, and ^{56}Fe ions in the energy interval 0-550 MeV/amu, whose resulting scintillation efficiency curves continue to rise with lowering stopping power, contrary to conclusions based on lower energy heavy ion data [E. Newman and F.E. Steigert, Phys. Rev. 118, 1575 (1960)]. An approximate phenomenological expression for heavy ion light output is offered that appears to be accurate to 20% for ion charge ≥2. A scintillation model is developed in which the primary dose distribution in the lattice undergoes diffusion and simultaneous "exciton-exciton" (second-order) annihilative interactions which quench part of the electronic excitation energy. This model provides an excellent qualitative fit to data spanning two orders of magnitude in stopping power and charges 1 to 26. Denial of the activator depletion hypothesis as a saturation mechanism receives a posteriori justification and explanation from the numerical results of this model.

In addition, response of NaI:Tl to cosmic ray muons and radioactive source γ-rays has been measured. Collectively, these measurements raise a number of unresolved questions regarding proton saturation and the mechanisms behind the observed decline in electron scintillation efficiency with decrease in stopping power.

---

*This work was supported by the Director, Office of Energy Research, Division of Nuclear Physics of the Office of High Energy and Nuclear Physics, Division of the U.S. Department of Energy under Contract No. W-7405-ENG-48.

†Also Space Sciences Laboratory

1. Introduction

In this paper we present data on the response of NaI:Tl, an activated alkali halide scintillator, to relativistic ^{20}Ne, ^{40}Ar, and ^{56}Fe ions in the energy interval 0-550 MeV/amu, provided by Lawrence Berkeley Laboratory's heavy ion accelerator, the Bevalac. These are to our knowledge the first published data on NaI:Tl response to relativistic heavy ions, all previous work being restricted to $E \leq 10$ MeV/amu.[1-9] The purpose behind the measurements was twofold. The first was to elucidate the mechanisms involved in the alkali halide (AH) scintillation process. It is well accepted that any successful model of AH response must take into account the distribution of energy deposited in the lattice about the path of the exciting particle. This "dose profile" or "track structure" varies significantly with the velocity of the projectile ion. Therefore, relativistic heavy ions could be expected to add substantially to our understanding of AH response mechanisms because their concomitant dose profiles are considerably different from those of low energy ions, and their dose levels are much higher than for relativistic, singly charged particles.

The second purpose was to extend the available NaI:Tl response data to relativistic energies for the benefit of those using AH scintillators in cosmic ray or nuclear physics detector systems. In this regard, a linear relationship between total light output L and a certain function of the projectile ion parameters, originally found to fit low energy data,[10] is found to apply to our data as well. This may prove quite useful for estimating NaI:Tl response where specific heavy ion data is unavailable.

In addition to the heavy ion data, measurements made of NaI:Tl response to ^{137}Cs γ-rays (662 keV), ^{241}Am γ-rays (59.5 keV), and cosmic-ray-produced atmospheric muons are presented. These measurements, taken by themselves, generally conform to the fairly well established electron response (L/ε, ε being the total energy) and efficiency ($dL/d\varepsilon$) curves calculated and measured by others.[12,13,11,14] However, the traditional placement of these curves relative to proton efficiency (frequently normalized to unity) are not nearly so well established, and in fact are called into question by our data. We give a review of the literature pertaining to this problem, but the disparity of results precludes resolution of this question.

Finally, we present a model of AH scintillation that achieves qualitative agreement with heavy ion data over the range $1 \leq Z_1 \leq 26$ (Z_1 = ion charge) and $2 \leq E \leq 500$ MeV/amu. In our model, the "prompt" ($<10^{-12}$ sec) energy dose profile in the lattice created by an ion of given charge Z and energy E is calculated. This energy then diffuses in the form of excitons. A decrease in scintillation efficiency occurs as a result of exciton-exciton (biparticle) interactions (favored in regions of high energy density) which end in a loss, or quenching, of electronic excitation energy. This model reflects the experimentally observed fact that scintillation quenching in AH's is independent of activator concentration and is solely a property of the pure (non-activated) crystal.[3,15]

The structure of the paper is as follows. Section II is devoted to the relativistic heavy ion data: the experimental configuration, method of analysis, and measurement of photomultiplier tube (PMT) linearity are discussed, and comparison is made with other heavy ion

data. This section supplies the high-stopping-power ($d\varepsilon/dx$) portion of the traditional $dL/d\varepsilon$ versus $d\varepsilon/dx$ plane. Section V describes our muon and γ-ray measurements, and reviews other experimental evidence relating proton to electron response. This section fills in the low $d\varepsilon/dx$ portion of the $dL/d\varepsilon$ versus $d\varepsilon/dx$ plane. Section III provides a brief review of some of the physical processes in AH's in preparation for Section IV, which details the dose calculation and scintillation model, along with its results.

II. Heavy Ion Data

A. Experimental Configuration

The experiment was conducted at LBL's Bevalac, during which several types of scintillators (mostly organic plastic and liquid), including a standard Harshaw Chemical Co. NaI:Tl crystal ($2\frac{1}{2}$" D x $\frac{1}{2}$" thick, Type D housing), were examined. In three separate runs, spaced 48 h apart, ^{20}Ne, ^{40}Ar, and ^{56}Fe ion beams of fixed energy (~600 MeV/amu) were directed onto the experimental apparatus shown in Fig. 1. Passage through an automated absorber consisting of eight extremely precise plates of thickness 2^n (n = 1, ..., 8), made mostly of a high-Z material (Pb) to minimize nuclear interactions during slowing, allowed us rapidly and nearly continuously to vary the ion energy entering the NaI:Tl crystal. A solid state (silicon) detector situated midstream discriminated against ions having undergone charge-changing nuclear interactions in the absorber. The NaI:Tl crystal, all but one face covered by an Al-Al_2O_3 housing, illuminated the interior of a light diffusion box. The interior of the light diffusion box was painted with a highly reflectant, nearly wavelength-independent powder, $BaSO_4$.[16,17] Light entering through a window (to which was attached the scintillator) was randomized through successive "bounces" during which original spatial information was lost. The constant fraction of the total light collected by the PMT was, therefore, nearly independent of the ion entry position at the scintillator face (much less than 1% by computer calculation[18]). Use of a light diffusion box also enabled us rapidly and reproducibly to change scintillator samples with assurance of a constant scintillator-PMT coupling efficiency.

The PMT used was an EMI9817Q tube with S-20 (trialkali) photocathode for low resistivity and distortion, a fused quartz (Spectrosil) window providing a spectral range of 165-850 nm, and a non-linear dynode chain to avoid space-charge effects at high anode current levels. To calibrate against tube gain drifts occurring during the course of the exposures, a calibration source of ^{241}Am-doped NaI:Tl with an activity of ~3 n Ci was prepared for us by Harshaw Chemical Co. The 5.49 MeV alphas emitted within this calibration crystal provided a constant light level that was adopted as the unit of light output; all signals are given in units of this source. Because of the temperature dependence of NaI response, the temperature was controlled so as to limit response variations to $\leq$0.4% over the three exposures. Tests of PMT linearity are discussed below. The PMT signals were amplified and stored in a Canberra (Omega 1) pulse height analyzer (PHA).

B. Method of Analysis of Heavy Ion Data

Each pulse height spectrum, consisting of ~10^4-10^5 individual ion pulses, was read to ~1-2 channel (ch) accuracy; afterwards these channel numbers were converted to give light outputs ΔL in units of our calibration source signal. To determine the total energy $\Delta\varepsilon$ deposited in the scintillator, the ion energy upon entering (E_i) and leaving (E_o) the crystal had to be calculated. (Throughout, a script ε denotes total energy with units of MeV; a capital E denotes energy in units of MeV/amu.) Assuming a known beam energy E_{top}, at the top of the experimental apparatus, a range-energy program integrated the energy loss through all the tabulated upstream matter in the beam line (including any absorber plate mass) to arrive at values for E_i and E_o.

The range-energy program[19] used in this procedure incorporated higher order corrections in Z_1 to stopping power[20] to provide an energy accuracy of <0.5%-1.0%[21] for the charges and energies used. Since the beam extraction energy from the accelerator was not known precisely, E_{top} was treated as a floating parameter which was fixed for each charge with excellent consistency during the data-fitting procedure described below.

Figures 2a-c show the "raw" response curves for Ne, Ar, and Fe. The shape of these curves is readily understood: as the entrance energy E_i decreases, dE/dx increases and more energy is deposited in the crystal before the ion exits through the interior crystal face, producing a higher light level ΔL. The cusp occurs at an energy where the particle is stopped just at the exit face of the crystal (maximum energy deposition), while for smaller E_i the ion stops within the crystal. To fit the data, the light response L of an <u>infinitely</u> thick crystal was taken to have the form $L = \sum_{k=1}^{n} a_k E_i^k$. This non-orthogonal polynomial expansion was chosen because L = 0 when E = 0 without requiring the imposition of a constraint equation on the coefficient parameters a_k. Thus, for an ion entering a finitely thick crystal with energy E_i and exiting with energy E_o, the light response is $\Delta L(E_i) = L(E_i) - L(E_o) = \sum_{k=1}^{n} a_k (E_i^k - E_o^k)$. Use of a least squares technique involved minimization of $\chi^2 = \sum_{\ell} \omega_\ell (\Delta L_\ell - \sum_k a_k \phi_{k\ell})^2$ with respect to the a_k coefficients, where the sum in ℓ is over all data points, ΔL_ℓ is the measured light output, ω_ℓ is a weighting factor, and $\phi_{k\ell} \equiv (E_{i\ell}^k - E_{o\ell}^k)$. The solution vector $\bar{a}$, however, is a function of the parameter E_{top} since that parameter determines the $E_{i\ell}$ and $E_{o\ell}$ values; a non-linear optimization method was used to converge quickly

on that value of E_{top} giving the minimum χ^2 in $\{\bar{a}, E_{top}\}$ space. This method of determining E_{top} was extremely consistent, giving a relative dispersion of $\sim 10^{-6}$ over several independent scintillators. The weighting function ω_ℓ gave weight to each datum point inversely proportional to the data point density. This way the fit in regions of sparse data was not sacrificed to excessive fitting in high data point density regions. The measurement σ's were assumed equal.

The resulting fits to the data are also shown in Figs. 2a-c. Once L(E) is known (Fig. 3), the scintillation efficiency (units of cal. source/MeV) follows immediately, $dL/d\varepsilon = (1/A_1)\,dL/dE$ (A_1 being the atomic weight of the ion in amu). These are shown in Fig. 4. Since L(E) is differentiated to provide the quantity of interest, the choice of polynomial order n is important. Figure 5a shows $dL/d\varepsilon$ vs E calculated for ^{56}Fe on NE110, a commercial plastic scintillator, where the polynomial order varies from 3 to 7. As seen, there is practically no sensitivity to n in the region $50 \leq E \leq 500$ MeV/amu, so the validity of our $dL/d\varepsilon$ values is assumed to be confined to this energy interval. Figure 5b shows χ^2 vs n; n = 5 was chosen as optimal. Beyond n = 5 the linear equation system becomes excessively ill-conditioned. (An F-test is not appropriate since the effective fitting errors are not normally distributed.) To estimate the influence of measurement error on $dL/d\varepsilon$, raw Fe data were augmented by a normal distribution of random numbers whose σ was comparable to the estimated error. The resulting variation in $dL/d\varepsilon$ was of the order of 1%, which when added to other sources of error gives an estimated total of ~2.5%.

C. PMT Test of Linearity

We now describe in some detail three complementary methods used to measure deviations from linearity of PMT response over five orders of magnitude of photocathode current, and over three orders of magnitude of anode current which represents the dynamic range of our measurements. This is particularly important since it affects conclusions regarding the relation of our low $d\varepsilon/dx$ data (muons, γ-rays) to our high $d\varepsilon/dx$ data (heavy ions). Our conclusion is that there is no evidence for photocathode saturation or for anode space-charge effects; however, decreased gain due to dynode heating is responsible for a total non-linearity of ~4% at the highest signal levels, with a non-linearity of ~3%-4% (i.e., relative variation of $\lesssim$1%) in the range of our heavy ion signals. The heavy ion data as a whole is corrected for this gain shift; however, the $\lesssim$1% gain variation within the heavy ion data itself is ignored since it is smaller than the effect of random errors on calculated $dL/d\varepsilon$.

For lower light levels the Poisson distribution of photoelectrons emitted at the cathode provides the first method for testing linearity. To see how linear response is verified, we consider the light source-PMT system as a system of three chained devices, A, B, and C. Device A consists of a precision pulser which drives an LED, illuminating the photocathode. Its output is photoelectrons. Device B is the dynode chain of the PMT, whose output is anode current. Device C consists of amplification electronics whose output is PHA channels. For two chained devices x and y with the mean gains m_x, m_y and variances σ_x^2, σ_y^2, the resulting mean gain and variance of xy is $m_x m_y$ and $(m_y^2\sigma_x^2 + m_x\sigma_y^2)$.[22] In our case, $m_A = \sigma_A^2 = N$ (number of

photoelectrons). Device B is more complex, itself consisting of a chained device, the dynode chain. For each dynode $m_i = \chi V_i$, i.e., the electron gain factor is proportional to the interdynode potential, and $\sigma_i^2 = (\chi V_i + b\chi^2 V_i^2)$, where b (the Polya parameter[22,23]) measures deviation of the dynode response from a Poisson process. Using the chain rule again we find

$$\sigma_B^2 \approx (\chi^k \prod_{i=1}^{k} V_i)^2 \left[b + (1+b) \sum_{i=1}^{k} \frac{1}{\chi^i} \prod_{j=1}^{i} \frac{1}{V_i}\right], \quad m_B = \chi^k \prod_{i=1}^{k} V_i,$$

where k = number of dynodes. Defining $K(V) \equiv 1 + \sigma_B^2/m_B^2$, we have $N = K(V) m_{AB}^2/\sigma_{AB}^2$. What we actually measure are m_{ABC} and σ_{ABC}; however, if we assume $\sigma_C = 0$ for the post-PMT electronics, then $m_{ABC}^2/\sigma_{ABC}^2 = m_{AB}^2/\sigma_{AB}^2$. Thus, we may measure N to within a constant K (which is close to unity) by measuring the spectrum peak channel and full-width-half-maximum (FWHM), where FWHM = $2.355\ \sigma_{ABC}$. (This last relationship is surprisingly accurate for the Poisson distribution.) Space charge saturation, for example, is immediately evident in a plot of N/K(V) vs peak channel number, since $N/K(V) \propto m_{AB}^2$ and peak ch $\propto m_{AB}$. (The variance σ_{AB}^2 is not sensitive to space charge saturation occurring in the last few dynodes, as seen by examining the expression for σ_B^2.) It is important in the above method to carefully subtract other sources of noise contributing to the spectrum width, especially at higher light levels where the relative FWHM is small. Figures 6a-c show linear tube response at three tube voltage levels.

For higher light levels the FWHM becomes too small to measure accurately, so a second method to measure PMT linearity was employed, this one using a rotating mirror assembly[24] (designed and built by a colleague, M. P. Budiansky) that is shown in Fig. 7. Continuous

light from a laser or lamp passes through a variable neutral density filter, enters the mirror assembly, and is alternately reflected off mirrors on the stationary walls and on the rotating mirror nut, finally leaving the assembly with an angular velocity 14 times that of the rotating nut. Because each exiting light pulse has been reflected off of only 7 of the 8 octagonal nut mirror surfaces, by making the reflectivity of each nut mirror different a repeated train of eight light pulses of differing magnitudes ensues. These relative amplitudes, being a property of the mirror reflectivities only, should remain in fixed proportion to each other. PMT saturation is then evidenced by a relative dminishing of the higher amplitude pulses of the eight-pulse train as the absolute light source intensity is increased. Results of this test are shown in Table 1; no saturation is evident at the intensities measured. Since the lowest light levels measured with this method overlap in intensity those signals measured with the first method, PMT linearity is so far confirmed.

Unfortunately, our strongest available light source for use in the above method was less by a factor of 30 than the maximum experimental light signal strength (^{56}Fe stopping in the NaI:Tl crystal). Thus a third method was employed to bridge this final region. In it, the PMT was directly exposed to the output of an LED fired by a precision pulser set at various voltage levels. The LED was fired again at the same levels after insertion of a baffle plate which reduced by orders of magnitude the light received by the PMT. Figure 6d shows the ratios of the baffle-out signals to the baffle-in signals. Saturation would be manifested as a drop in baffle-out/baffle-in ratio with increase in signal strength. To within ±1% no

saturation due to either excessive photocathode current or space-charge effects is observed. However, long-term gain drifts were observed at these highest light levels which were attributed to gradual dynode heating. Reproduction of original experimental conditions (a flux, with no temporal microstructure, of 10^3-10^4 ions/sec) showed a decrease in PMT gain occurring over a few seconds of LED emission which produced a net 3-4% decrease in our measured calibration signal. Cessation of signal resulted in a gradual cooling over several seconds to the original tube gain. Dynode heating was concluded to be the cause due to the time periods involved, and also because the drift was not continuous but occurred in jumps which indicated successive efficiency drops in neighboring dynodes. As described above, this calibration signal drop was corrected for in the heavy ion data.

D. Comparison with Other Data

Shown along with our data in Fig. 4 is the extensive low energy (1-10 MeV/amu) heavy ion data of Newman and Steigert (NS).[1] A salient feature of both sets of data is the separation of the efficiency curves for each charge; for a given stopping power, the larger charge has the higher efficiency. This is unequivocal evidence for the important role the distribution of dose energy in the lattice plays in scintillation response; regions of higher energy density have a reduced efficiency due to ionization quenching. Lower velocity particles tend to deposit more energy in the track "core," a high energy gensity region immediately about the projectile trajectory, than do higher velocity particles which produce greater numbers of high-energy secondary electrons (δ-rays) which transport energy to

regions of low energy density. Since $d\varepsilon/dx \propto Z_1^2/\beta^2$ (β being the ion velocity in units of c), the efficiency curve separation is then expected. The role of ionization quenching is corroborated in Fig. 8. Here our $dL/d\varepsilon$ data for Ne, Ar, and Fe are shown versus E, or equivalently, velocity. For a given velocity, the dose profile is roughly independent of charge, apart from an overall factor of Z_1^2. The unambiguous drop in average efficiency with increase in Z_1 attests to the enhanced role of ionization quenching due to this Z_1^2 factor in the dose profile. It should be pointed out that although the relativistic Ar curve as shown in Fig. 4 lies <u>above</u> the Fe curve, this separation is not significant, being within estimated errors; in fact, the separation should be in the other direction.

To cross-calibrate our data with those of NS, we made use of a parameterization by Womack et al.[10] They noticed that nearly all the data of NS for $Z_1 \geq 2$ fall on a single straight line when expressed as L versus $\in \propto \beta_0^3 A_1/Z_1^{2/3}$, β_0 being the velocity of the ion entering the (infinitely thick) crystal. (A similar relation was found for CsI:Tl data.[25]) We have found that this relationship is maintained with our data as well, with the relativistic Ne, Ar, and Fe data nearly falling on a common straight line. By assuming that a single line fits both sets of data as shown in Fig. 9, a calibration factor is determined that connects both sets of data. The validity of this procedure is seemingly confirmed by the resultant smooth "joining" of the two ^{20}Ne curve segments in Fig. 4. That this linear parameterization, which takes no ostensible account of track structure, holds for all charges over three orders of magnitude light output is quite remarkable and provocative. Being unable to explain its apparent

success, we merely emphasize its potential use to experimentalists while issuing the caveat that its estimated accuracy of 10-20% is based on limited data.

A prominent feature of the original NS heavy ion data is the near discontinuity of slope of each ion's efficiency curve at ~7 MeV/amu, where a constant, plateau value is reached as indicated in Fig. 4. The relativistic data indicate that the ion efficiencies in fact do not level off, but continue to rise with a gentler slope as $d\varepsilon/dx$ decreases. That a sudden shift in efficiency slope occurs at this velocity for all charges, however, is corroborated by Blue and Liu,[3] who measured proton and alpha efficiencies in unactivated (77° K and 300° K) LiI, NaI, KI, RbI, and CsI. In all but one case they observed an abrupt discontinuity in alpha efficiency at ~6 MeV/amu. They concluded that since this phenomenon was independent of ion charge, activator concentration, temperature, and even alkali type, it involved a velocity effect with the iodine atom. A possible explanation is that at this velocity an effective adiabatic cutoff for excitation of an inner shell iodine electron occurs, thus depriving the crystal of high-energy Auger electrons which transport a considerable fraction of the original excitation energy into low-energy-density, high-efficiency regions of the crystal. A velocity-dependent inner-shell excitation cutoff would then introduce a sudden decrease in efficiency because the remaining excitable shell electrons deposit their energy closer to the less-efficient core. (However, it is also possible[26] that this suggested effect would be opposed at low enough velocities by a Fano-Lichten mechanism[27] whereby inner shell electrons are excited as a result of exchange during transient projectile

ion-lattice ion molecule formation.)

Figure 10 combines additional NaI:Tl response data to give a broader picture of NaI:Tl behavior. (Only the high $d\varepsilon/dx$ points will be discussed here; the low $d\varepsilon/dx$ points are discussed in Section V.) Measurements by Eby and Jentschke[2] with protons (○) and alphas (●) show protons to have a constant efficiency, while alpha efficiency begins to drop from the proton $dL/d\varepsilon$ value for $\varepsilon \lesssim 20$ MeV. While several other experiments collectively indicate a constant proton efficiency over the energy interval 60 keV-100 MeV by virtue of their proton L vs ε points falling on a straight line passing through the origin (a positive energy offset indicates low-energy saturation), they do not all overlap or assure in any other way a common absolute scintillation efficiency. Therefore, the graphical placement of all proton points on a single $dL/d\varepsilon$ value in Fig. 10 should be viewed cautiously. Additional skepticism is due because, as shown, low energy protons have a higher efficiency than alphas of the same stopping power, in direct contradiction to all scintillation models incorporating track structure effects. Perhaps the strongest evidence against constant proton $dL/d\varepsilon$ is the careful experiment of Gwin and Murray[15] where proton efficiency was found to be non-linear in CsI:Tl (short dash-long dash line in Fig. 10).

The combined heavy ion data are normalized with respect to protons by use of an alpha point (▲) of NS whose energy $\varepsilon = 40$ MeV places it at maximum (proton) efficiency according to the results of Eby and Jentschke[2] and Blue and Liu.[3] On the whole, the $Z \geq 2$ data suggest that not only do alphas attain proton efficiency at low enough $d\varepsilon/dx$, but also heavier ions do as well. The relativistic ^{20}Ne curve nearly

reaches proton efficiency, and the ^{40}Ar and ^{56}Fe curves show no indication of not doing so (or coming as close as possible before minimum ionization energy is reached). A complete set of heavy ion scintillation efficiency curves then quite likely appears as a fairly tight band of lines departing from maximum (proton) efficiency with gentle slope, with each ion then breaking away at ~6-7 MeV/amu into a steeper drop in efficiency with $d\varepsilon/dx$.

III. Basic Processes in Alkali Halide Scintillation

We briefly review now some of the mechanisms involved in pure alkali halide (AH) scintillation and in activated AH scintillation before discussing models of scintillation. For more detailed discussion of pre-1964 work, the encyclopedia ref. 28 is recommended. A few papers which provide effective overviews of activated AH response are refs. 29, 30, 31, and 32.

When pure or activated (i.e., doped with ~0.0013 mole fraction Tl) NaI is excited by charged particles or photons, free electrons (e) and holes (h) are produced in the Na-3s conduction band and I-5p valence band, respectively, across a bandgap of ~5.8 eV. Recombination of the e-h pair within the pure lattice results in fluorescence at low temperatures. This process occurs in steps; within 10^{-13}-10^{-12} sec[33] a hole is "self-trapped" in the lattice by dropping into a level a few eV above the valence band to form a "V_K center." This type of center was determined by ESR studies[34] to be a hole locally shared by two adjacent halogen ions, forming a molecular ion. Polarization studies[35] showed that V_K centers migrate by hopping across an activation barrier to neighboring halogen pair sites, resulting in a dramatic decrease in diffusion coefficient (~10^{-5} cm/sec for V_K centers compared to ~10^{-1} cm^2/sec for free holes). Eventual recombination with a conduction band electron forms a "self-trapped exciton" (STE) similar to a Frenkel exciton. From this state radiative decay occurs at low temperatures. At higher temperatures (eg 300° K) non-radiative decay processes[36] dominate and severely reduce luminescence,[37] making pure AH's very poor scintillators at room temperature.

Doping the crystal with an activator such as Tl dramatically

enhances room temperature luminescence since it acts as a trap for both electrons[34,38] and holes/V_K centers,[32] thereby severely curtailing the STE formation channel which provides essentially no luminescence. Trapping of e or h at a Tl site causes a change from the original +1 charge state of Tl in the NaI crystal: $e + Tl^+ \rightarrow Tl^o$, and $h + Tl^+ \rightarrow Tl^{++}$. Most electrons, with their large diffusion coefficient of ~0.3 cm^2/sec,[30] quickly trap via $e + Tl^+ \rightarrow Tl^o$. Since holes rapidly self-trap in the lattice, only a small fraction "promptly" trap[32,31] via $h + Tl^+ \rightarrow Tl^{++}$ (see footnote 39) while the remainder slowly diffuse as V_K centers, eventually trapping via $V_K + Tl^+ \rightarrow Tl^{++}$ or $V_K + Tl^o \rightarrow Tl^+ + h\nu$.[40] The latter process, resulting in characteristic fluorescence, has been shown to be an important contributor to the scintillation process.[41,31] The second process which contributes to fluorescence is $e + Tl^{++} \rightarrow Tl^{+*} \rightarrow Tl^+ + h\nu$, where Tl^{+*} is the excited state of Tl^+ (with decay time ~0.22 μsec[42]). Unlike holes which are deeply trapped in Tl^{++} ions and do not escape thereafter, electrons are rather shallowly trapped in Tl^o ions and do escape into the conduction band with significant frequency above a certain temperature (the thermoluminescence peak temperature[32]). From there, they either retrap ($e + Tl^+ \rightarrow Tl^o$) or combine with Tl^{++}, leading to radiative decay. This process continues until all electrons and holes have recombined, completing the scintillation process.

A question that pertains particularly to low $d\varepsilon/dx$ crystal response but that is also relevant to high $d\varepsilon/dx$ behavior is that of recombination kinetics. Do electrons and holes (whether they be free or trapped) recombine according to first order or second order kinetics? A second order recombination rate, i.e., $dn/dt = -K_2n^2$ (n = e-h density)

implies that the electron and hole distributions are independent of one another, while a first order rate $dn/dt = -K_1 n$ implies that the electron and hole in each pair are spatially correlated and recombine with a rate constant K_1 independent of the total pair density. A second order recombination process has an effective decay time that is dependent upon time and initial dose, viz., $dn/dt = -K_2 n(0)^2/[1+K_2 n(0) t]^2$, while a first order process has a constant decay time. For scintillation detection systems with finite integration times one expects, should second order kinetics hold, that as the initial e-h pair density (i.e., $d\varepsilon/dx$) declines the integrated fraction of the total ($t \to \infty$) signal will decline, resulting in an apparent drop in scintillation efficiency at lower $d\varepsilon/dx$. This is in fact observed (Figs. 10,17) in the electron efficiency curve. Assuming a negligible role for ionization quenching at these pair densities, the measured electron efficiency curve is nearly reproduced by $dL/d\varepsilon \propto 1 - n(\tau)/n(0) = 1 - n(0)/[1+K_2 n(0)\tau]$, where $n(\tau)$ is the second order kinetics solution for pair density at the detector integration time τ (see Fig. 11). Also, one expects from second order kinetics that the average signal decay time will increase as $n(0)$ decreases. From rough measurements in our lab, we found scintillation decay times (measured off the PMT anode) for ^{241}Am α's, ^{137}Cs γ-rays, and atmospheric muons to be 0.20 ± 0.02 μsec, 0.28 ± 0.03 μsec, and 0.30 ± 0.05 μsec respectively, confirming this effect.

However, Kaufman and Hadley[43] using X-rays in KI provide evidence that the e and h in a pair do remain spatially correlated at low pair densities, either through Coulomb interactions or simply by virtue of being trapped at neighboring Tl sites. (At high pair

densities they conclude that the e and h distributions do become independent, presumably because with large enough dose the average separation between e-h (correlated) pairs is comparable to the e-h distance within a single pair.) Aluker and Lusis[44] using UV excitation have demonstrated the increasing separation of e and h with increase in photon energy. This suggests that in fact a continuum of degree of correlation exists, and that the low correlation end of the spectrum substantially contributes to efficiency decline when the initial dose is small enough so that individual pairs are widely separated.

At high values of $d\varepsilon/dx$ the phenomenon of "saturation" occurs, leading to a drop in scintillation efficiency (Fig. 10). Various mechanisms have been proposed to explain this decline. Some models invoke depletion of activator sites as being responsible[45,46,47]: as the e-h pair density increases, the crystal's supply of unoccupied Tl sites becomes exhausted, and the remnant e-h pair density cannot contribute to scintillation for lack of available Tl sites. Though highly plausible, this mechanism has been convincingly disproved by the work of Gwin and Murray[15] and Blue and Liu[3]; apparently saturation is a property of the pure lattice only. Other models attribute scintillation efficiency decline to "ionization quenching"[48,50,49]: in regions of high energy density, certain (unknown) non-radiative decay channels become efficient and depopulate much of the electronic excitation. These channels may include direct exciton-exciton annihilation, formation of quenching centers (e.g. transient F-centers[51,52]) which destructively interact with excitons, or enhanced probability for electron-hole recombination into exciton

states which are either very short-lived or nearly immobile.

An inescapable conclusion that comes with rejection of the activator depletion hypothesis is that two or more excitons cannot coexist within the effective capture volume of a Tl^+ ion. (From here on, we use the term "exciton" in a generic sense, applying it even to a V_K center with a spatially correlated electron.) Were this possible, one exciton would occupy the Tl site, leaving the others ineffective with respect to luminescence, which is simply activator depletion. Instead, an annihilation process must effectively reduce the exciton density below a level whose upper limit is provided by the inverse of the Tl^+ effective capture volume. This capture volume can be roughly estimated using experimental data on light output L for γ-rays (low $d\varepsilon/dx$) versus Tl concentration[53] which has been found to fit a theoretical expression by Johnson and Williams[54] for scintillation efficiency versus Tl concentration, $dL/d\varepsilon \propto c(1-c)^m/[c+(\sigma_\ell/\sigma_a)(1-c)]$. Here c = mole fraction of the activator, σ_ℓ/σ_a is the ratio of exciton capture cross-sections for the lattice and activator ion, and m is the number of immediately surrounding alkali sites which must be free of Tl ions to avoid concentration quenching (which occurs when the close proximity of a Tl^+ ion enables it to interact and interfere with the fluorescent decay of a neighboring Tl^{+*} ion). Neglecting the concentration quenching factor $(1-c)^m$, an identical form can be achieved with a different physical model in which we assume each activator site to have an effective capture volume V. As the density N of activator ions is increased, the total capture volume corresponds to an effective activator density $n = N/(1+NV/2) \propto dL/d\varepsilon$. The less than linear increase of n with N is due to random overlap of

individual ion capture volumes. Fitting this function to the data, one obtains $V \approx 1.2 \times 10^6$ Å^3, giving a capture radius of ~66 Å.

This capture radius happens to be of the same order of magnitude as estimates of the exciton lifetime diffusion length, ~10^2 Å. Experiments where excitons were used to ionize F-centers in RbI films[55] demonstrated a lifetime diffusion length of ~100 Å. (This experiment also indicates a non-radiative decay channel for excitons.) Nishimura and Tomura[56] also demonstrate exciton diffusion in KI, with an (extrapolated) room temperature diffusion coefficient of ~10^{-3}-10^{-4} cm^2/sec. This matches the above estimate of diffusion length well when combined with the measured exciton lifetime in room temperature NaI, 15 nsec.[37] It is tempting to treat the Tl capture radius as further evidence that the exciton's lifetime diffusion length is ~10^2 Å, implying that exciton-exciton annihilation processes (the term now being employed generically to cover all second order annihilative processes) are very efficient if activator depletion is not to be observed.

The hypothesis of exciton-exciton annihilation is supported by recent time-resolved spectroscopy of exciton emission in $KMnF_3$. Strauss et al.[57] measured the magnitude of a second order decay channel that yielded no luminescence, indicating the existence of an annihilative exciton-exciton process. In work in photosynthetic membranes, for example, it is generally accepted that singlet-singlet exciton annihilation occurs, and models which incorporate this interaction successfully explain noted fluorescent behavior.[58] As mentioned above, another possible channel for non-radiative decay is through ionization of F-centers. Since excitons and transient F-centers

(whose production rate is orders of magnitude larger than permanent F-centers[51]) apparently transform into each other in the lattice,[51,59,60] this decay channel can be equivalently considered an exciton-exciton annihilation process. Although other species of quenching centers may possibly be formed in the lattice at high energy density, we have no knowledge of what these may be, if they indeed exist. Therefore, in our model of scintillation we assume saturation to be primarily due to a second-order, non-radiative decay process.

IV. Model of Scintillation

Several models have previously been proposed to explain inorganic scintillation behavior. Birks[48,28] offered a relation for absolute scintillation efficiency where ionization quenching is accounted for phenomenologically by the factor $(1 + B d\varepsilon/dx)^{-1}$, which allows a fit to the general trend of $dL/d\varepsilon$ versus $d\varepsilon/dx$. In a more sophisticated treatment, Murray and Meyer[45] assumed diffusion of excitons from a line source with competitive trapping at fixed activator sites and fixed lattice traps, whose nature is unspecified but acts to remove excitons from the system. Their solution curve nicely reproduces the trend of $dL/d\varepsilon$ versus $d\varepsilon/dx$ over four orders of magnitude in $d\varepsilon/dx$, although, as in Birks' formula, $dL/d\varepsilon(d\varepsilon/dx)$ is a monovalued function that cannot explain charge separation of the efficiency curves. (This was corrected for later[11] by inclusion of the effect of high-energy δ-rays of assumed unit scintillation efficiency.) The underlying hypothesis of activator depletion, however, was shown to be faulty when subsequent experiments by Gwin and Murray[15] showed that the shape of the efficiency curve is independent of activator concentration, contradicting a conclusion of the Murray and Meyer model.

Katz and Kobetich[46] resurrected the activator depletion hypothesis by assuming that sensitization (excitation) of an activator site obeys a cumulative one-or-more-hit Poisson distribution, so that the probability for sensitization of a given activator ion in a region of local energy density g is $P = 1 - \exp(g/g_0)$, where g_0 is a dose parameter. The dose profile g(r) (r = radial distance from the ion trajectory) was calculated using the differential energy production cross-section for δ-rays and electron range-energy relations.[61]

Their results overall impressively match the experimental data of Newman and Steigert[1] (NS); this is undoubtedly due in part to their careful attention to the dose profile calculation. For those few ions where theory and experiment do not meet, an extension of the Katz and Kobetich model by Ladu et al.[47] provides a much better fit. However, the Katz and Kobetich model predicts a decrease in heavy ion $dL/d\varepsilon$ for lower $d\varepsilon/dx$, $\sim 5 \times 10^2$-5×10^3 MeV-cm^2/g, in contradiction to our experimental results.

Luntz[50] emphasized the importance of ion velocity as opposed to ion $d\varepsilon/dx$ in his scintillation model which assumes a dose $g \propto 1/r^2$ up to a radius determined kinematically by the range of a maximum energy δ-ray. Above a critical radius r_c luminescence is linear with energy deposition; below this radius nonradiative competitive processes effectively quench all excitation energy. His model reproduces the general behavior of the NS heavy ion data, although to obtain this fit it was necessary to make his model parameters charge dependent.

Recognizing the importance of the dose profile as evidenced by the models of Katz and Kobetich and of Luntz, our model of scintillation includes a detailed dose calculation described in the next section. Unlike the Katz and Kobetich calculation, in our total dose we include excitation energy which is not transported away from the core. Unlike Luntz, we do not distinguish regions of high and low efficiency, but instead directly calculate loss of excitation energy due to second order (exciton-exciton) processes. Incorporation of exciton diffusion into the model allows some of the excitation energy to migrate away from the core and have an enhanced survival probability. All of the energy remaining after approximately 10^{-8} sec (exciton lifetime) is

assumed to be coverted to luminescence, i.e., the scintillation efficiency is simply the fraction of the initial total energy that survives exciton-exciton annihilation. The numerical results of our model validate a posteriori this assumption that is equivalent to a denial of the activator depletion hypothesis.

A. The Dose Profile

The accurate determination of dose distributions from ionizing radiations or from heavy ions is an important problem in biophysical and biomedical research, and much work has been done in this area (e.g., refs. 61-63). In a representative calculation, Faïn et al.[62] determine the total secondary electron differential energy spectrum by calculating for each electron shell of the absorbing medium a velocity distribution of electrons which interact with the projectile ion according to a classical collision theory. Monte Carlo calculations of subsequent δ-ray energy deposition ultimately yield a dose away from the core that drops as $1/r^2$. The Bethe theory of energy transfer is used to calculate core doses, and these two components are added together to yield the total dose profile.

Our dose calculation is simpler, but along similar lines. In our computer computation, the dose (histogram) profile is calculated by evaluating the energy deposited in annuli about the ion trajectory. The boundaries of the annuli are evenly spaced logarithmically from $R = 10^{-5}$ Å to 10^{+8} Å, with 10 annuli per decade in radius. A very small lower limit is required to obtain close collisions with energy transfers near the kinematic limit, and the large upper limit corresponds to the range of the maximum energy δ-ray produced for the ion energies under consideration. We determine our sampling radial

coordinates r_k within each annulus of lower boundary R_k by requiring $\pi(R_{k+1}^2-R_k^2)g(r_k) = 2\pi \int_{R_k}^{R_{k+1}} rg(r)dr$, where $g(r)$ is an analytic expression for the primary dose that is generally $\propto 1/r^2$. This condition gives $r_k = ((\lambda^2-1)/2\ell n\lambda)^{\frac{1}{2}} R_k$, $\lambda = 10^{0.1}$.

The contribution to the total dose profile from each electron shell of the NaI molecule is calculated separately, using the ionization potentials I_i and oscillator strengths f_i given by Sternheimer[64] (see Table 2). The electron shells are divided into two classes: "local" shells, in which the electronic energy of a barely ionized shell remains in the region occupied by the excited molecule, and "nonlocal" shells, in which subsequent Auger emission or X-ray fluorescence transports a significant fraction of the ionization potential energy away from its point of origin.

In both classes of shells, a close collision with the ion results in a high energy δ-ray of energy $\omega = \varepsilon - I$, where ε is total energy transferred during the collision and I is the ionization potential of the shell. Electron ejection perpendicular to the ion trajectory is assumed, an excellent approximation for all but the highest energies. Energy deposition in the crystal by slowing δ-rays is calculated using an empirical electron range-energy relation $r(\omega) = 236\ \omega^{1.5}$ Å (ω in keV). This relation was determined by fitting the data of Katz and Penfold[65] for the practical range versus energy for electrons in Al (see also ref. 61) to a power law. A constant correction factor was introduced to account for the difference in electron ranges between Al and NaI (cf. tables in ref. 66). Also, the transmission fraction function of Rao[67] was used to convert practical range to 50% transmission range so that the <u>average</u> slowing behavior of electrons is

reproduced. The energy deposited by a δ-ray produced at r_ℓ with energy ω' in annulus k is then $\Delta\omega = \omega(r(\omega')+r_\ell-R_k) - \omega(r(\omega')+r_\ell-R_{k+1})$, where $\omega(r)$ is the inverse of $r(\omega)$.

The primary energy transferred to a shell electron during a collision is calculated using the results of Bohr[68] who found the energy transfer to a harmonically bound electron of frequency $1/\hbar$ by a passing ion of charge Z_1, velocity βc, and impact parameter b to be

$$\varepsilon(b) = \frac{2Z_1^2e^4}{m_e c^2\beta^2 b^2}\left[\xi^2K_1^2(\xi)+\xi^2K_0^2(\xi)/\gamma^2\right],$$ where m = e^- mass, $\xi \equiv (1b/\hbar c\beta\gamma)$, $\gamma = (1-\beta^2)^{-\frac{1}{2}}$, and $K_0(\xi)$, $K_1(\xi)$ are modified Bessel functions. (See also Jackson[69] for a clear discussion of collisional energy transfer.) Ahlen[20] has advanced arguments for the continued validity of the above expression down to impact parameters well within the atomic volume, in fact down to $b^q_{min} = \hbar/\gamma mc\beta$ when $Z_1\alpha/\beta < 1$, where $\alpha = e^2/\hbar c$, and b^q_{min}, being the wavelength of the scattered electron, represents the smallest impact parameter meaningful in a classical sense. At extremely small "impact parameters," ε(b) approaches asymptotically $\varepsilon_{max} = 2mc^2\beta^2\gamma^2$, the kinematic limit to energy transfer. To join the Bohr expression, $\propto 1/b^2$, to the constant, maximum energy transfer value, an intermediate curve segment $\propto 1/b$ is inserted at points b_1 (connecting to ε_{max}) and b_2 (connecting to the Bohr formula) to give a single expression for energy transfer,

$$\varepsilon(b) = \varepsilon_{max}\left(\frac{b_1}{b+b_1}\right)\left(\frac{b_2}{b+b_2}\right)\left[\xi^2K_1^2(\xi) + \xi^2K_0^2(\xi)/\gamma^2\right],$$ where

$b_1b_2 = \left(\frac{Z_1e^2}{\gamma mc^2\beta^2}\right)^2$. The parameter b_2 (and hence b_1) is determined by requiring the sum of ε(b) over all electrons to be equal to total dε/dx as given by the Bethe-Bloch formula.[20]

Using this expression, the mean energy transfer ε to a given shell electron at the sampling coordinate of an annulus is calculated. If $\varepsilon > I$, every shell electron in the annulus is excited and propagates outward as a δ-ray of energy $\omega = \varepsilon - I$. If $\varepsilon < I$, then ionization is assumed to occur in the fraction (ε/I) of electrons, the remainder being unexcited. The ionized electrons in this case are assumed to have energy $\omega = 0$, although integration over low-velocity ionization cross-sections[70] gives a mean electron energy of up to $\omega = 0.12\ I$.

Excited inner shells decay either through Auger electron emission or through X-ray fluorescence, with the relative probability of fluorescence being $p_x = (1+aZ_2^{-4})^{-1}$[71] where Z_2 is the atomic number of the absorber atom and a is a shell-dependent parameter. X-ray fluorescence is significant only for the iodine K shell (88%). Ionization of the iodine L shell, for example, is followed by Auger emission leaving two M shell vacancies; these are followed by N → M Auger transitions, etc., until only shells of ionization potential <0.1 keV are left empty, these being assumed not to contribute to further energy transport. As an approximation to isotropic emission, Auger electrons are emitted at 45° in our model. Table 2 gives the fraction Ω of initial ionization potential energy left behind in each shell after these processes. $\Omega < 1$ for "nonlocal" shells and $\Omega = 1$ for "local" shells. Figure 12 shows a typical dose profile calculated with this model.

B. Kinetics

The prompt dose distribution as described above provides the $t = 0$ initial conditions (for a given ion charge and velocity)

for subsequent kinetic evolution. To facilitate computation, the exciton diffusion equation $\partial g/\partial t = D\nabla^2 g$ for a cylindrical geometry was re-expressed as $\partial g_i/\partial t=(D/r_i^2)[g_{i+1}-2g_i+g_{i-1}]/(\ell n\lambda)^2$, where $\lambda = r_{i+1}/r_i$. To minimize machine-loss of total energy during computational diffusion, the annuli sampling coordinates r_k were recalculated for a dose profile $g \propto 1/r^2$, giving $r_k = \lambda^{\frac{1}{2}} R_k$. "Diffusion losses" were kept to less than a few percent and in all cases were accounted for. An efficient algorithm for stiff systems of orginary differential equations[72] was used to integrate our coupled equations $\partial\bar{g}/\partial t = G(\bar{g})$.

The very high densities calculated for $r < 1$ Å are deceptive in that the axial separation between excitons may be far larger than $g^{-1/3}$, the average separation in a homogeneous system; calculation of second order (g^2) processes using these high densities would yeild an unphysically high degree of interaction. Instead, the densities at small (<3 Å) radii were allowed to homogenize via diffusion until the axial separation between excitons became equal to the radial width of the homogenized dose (≥3 Å). Only then were other interactions turned on. Exciton density is determined by the assumption of 20 eV/exciton.

At this time, before further temporal evolution occurred, the exciton population was reduced via a process that is mathematically identical to the quenching factor of Katz and Kobetich[46] although of different physical origin. In the model, exciton density reduction occurs because a single NaI molecule can accommodate only a limited number of excitons. If the exciton density exceeds this limit, the excess is presumed to be promptly quenched in some (unknown) manner. Mathematically, if there are M sites for m particles, with the probability of a given site receiving a given particle being 1/M, the

mean number of occupied sites is $M[1-\exp(-m/M)]$, giving each exciton a survival probability of $[1-\exp(-m/M)]$, where m is proportional to the local dose g. If we were to postulate no further kinetic evolution, with all extant excitons contributing to luminescence, our results would be identical to Katz and Kobetich's (apart from the dose calculation) upon equation of M with their characteristic dose g_o (although their derivation employs the activator depletion hypothesis whereas our does not). However, their g_o corresponds to an accommodation factor orders of magnitude lower than that used in our model, one exciton per two NaI molecules. This sudden, one-time exciton loss contributed from 0% to 40% of the total energy loss to quenching depending upon ion charge and velocity.

Further exciton loss resulted only from exciton-exciton annihilation as continued evolution obeyed the kinetics equation $\partial g/\partial t = D\nabla^2 g - Kg^2$. Integration was continued up to $t = 10^{-8}$ sec, corresponding to the exciton lifetime, and ratios of remnant total energy to initial total energy were computed and equated to scintillation efficiency $dL/d\varepsilon$. Because of the high computational cost of doing so, loss terms in the dose differential equations corresponding to capture at activator sites and decay within the lattice were not included. Instead, the exciton decay (measured lifetime of 15 nsec) was approximated as a step function at $t = 10^{-8}$ sec. Implicit in our treatment is the assumption that a constant fraction (dependent upon activator concentration but independent of initial dose) of the remaining excitons just before decay at $t = 10^{-8}$ sec are trapped at activator sites and contribute to luminescence. Therefore, the activator sensitization efficiency is certainly somewhat

underestimated, because the model does not allow sensitization while $t < 10^{-8}$ sec, during which dose values are higher. However, since the sensitization rate is $\propto g$ while the quenching rate is $\propto g^2$, this should not be too unreasonable an approximation.

C. Results

The three parameters in our model are the exciton diffusion coefficient D, the biexciton annihilation rate K, and the number of NaI molecules required to accommodate one exciton, η. Computational expense made impossible a thorough mapping of K-D-η space over a wide range of ion charges and energies. Instead, with η set to zero, the K-D plane was searched and a locus determined ($K \propto D$) for which a 2.5 MeV alpha particle registered the experimentally observed degree of saturation. Then a complete set of $\{Z_1,E\}$ scintillation efficiency points were calculated for selected positions on the K-D locus. Little variation in the resulting efficiency curves occurred over the K-D locus, giving us the freedom to choose $D = 10^{-4}$ cm^2/sec as being most consistent with experimental data,[56] thereby fixing K at $2 \times 10^{-10} \frac{cm^3}{keV\text{-}sec}$. A small degree of fine tuning thereafter resulted in a choice of $\eta = 2$.

In Fig. 13 the results of the model with these parameter values are compared to the proton and alpha data of Eby and Jentschke,[2] the heavy ion data of Newman and Steigert,[1] and our relativistic heavy ion data. Given the limited ability to optimize our fit by parameter variation, and given the crude step-function nature of our model's activator sensitization and exciton decay, the degree of fit over more than two orders of magnitude in $d\varepsilon/dx$ is impressive. Qualitatively, where not quantitatively, all experimentally observed features are

reproduced. The degree of separation between the ^{20}Ne, ^{40}Ar, and ^{56}Fe efficiency curves closely follows our data. The alpha data also agree well with experiment. The proton points lie somewhat above the experimental value as a result of normalization of all calculated curves to allow matching of model and experiment at the 50 MeV/amu ^{20}Ne point. A slight degree of proton saturation is predicted by the model which very well may not have been detected by experiments in NaI, but which is strongly suggested by observation of proton saturation in CsI.[15] The poorest fits occur for the NS data, and even there the calculated efficiencies are never off by more than one charge unit (e.g., the 8 MeV/amu ^{16}O calculated efficiency nearly falls on the experimental ^{14}N curve). The most glaring deficiency is that the calculated low-energy heavy-ion slopes are not as steep as the NS data indicate. Part, though not all, of this discrepancy may be explained by noting that some of the stopping powers as calculated by NS for the lower of their measured heavy ion energies are too low. Correcting for this would somewhat decrease the slopes of their experimental curves.

As discussed earlier, abrupt shifts in efficiency curve slopes have been observed to occur at ~6 MeV/amu. The ^{20}Ne calculated curve shows such a slight shift at ~10 MeV/amu, as does the ^{4}He curve. We have not directly explored, however, the hypothesis that effective adiabatic cutoff of iodine inner shells is responsible for this observed shift.

One remarkable result of our model is an explanation for the absence of activator depletion as a mechanism contributing to saturation. As stated earlier, the absence of activator depletion implies

an annihilation process so efficient that two excitons cannot coexist for an exciton lifetime within the capture sphere of a Tl^+ ion (whose radius is probably determined by the exciton lifetime). Our numerical results show that for all charges and energies, the maximum dose value just prior to activator sensitization at $t = 10^{-8}$ sec is always comparable to or less than the equivalent of one exciton per Tl^+ capture sphere volume. We emphasize that this is not a priori a necessary outcome of our model, although it does provide a posteriori justification for our neglect of activator depletion as a saturation mechanism. That this felicitous upper limit on final dose ensues in an independent manner as a result of fitting calculated efficiency curves to data strengthens confidence in the underlying bases of this model.

We stress that the striking qualitative match between model and experiment over two orders of magnitude of $d\varepsilon/dx$ and for charges of $Z_1 = 1$ to 26 has not arisen from a careful selection of our three charge and energy-independent parameters. The qualitative features shown in Fig. 13 are actually impossible to avoid with this model; variation of parameters usually simply shifts the curves up or down as a whole (with minor relative displacements between separate curves) with "squashing" at the 1.0 or 0.0 scintillation efficiency limits. This feature is quite fortuitous, since even a modest sensitivity of global efficiency behavior to the chosen parameters would have made it difficult, if not impossible, to converge on a reasonable fit given computational limitations. This characteristic of the model, along with its independent internal consistency with regard to activator depletion, strongly supports the validity of its elements.

V. Low Stopping Power Scintillation Efficiency

Along with the relativistic heavy ion measurements, we made a measurement of scintillation efficiency for cosmic-ray-produced atmospheric muons. Figure 14 shows the experimental configuration which consists of the same crystal + light-diffusion box system as used in the heavy ion measurements, along with two additional scintillators. Three-fold coincidence from these scintillators was required for gating of the input; this limited muons to those of nearly vertical pathlength, suppressing crystal pathlength variations to <1%. Six inches (27 radiation lengths) of Pb above the bottom coincidence scintillator screened out all cosmic ray electrons whose severe energy loss fluctuations would otherwise contaminate the muon spectrum. The Pb also limited detected muons to energies ≥250 MeV. The resulting pulse height spectrum is shown in Fig. 15. At these very high energies, $dL/d\varepsilon = \Delta L/\Delta\varepsilon_p$, where ΔL is the peak light output, and $\Delta\varepsilon_p$ is the most probable energy loss (not the mean loss, since the Landau distribution[73,74] holds here). Figure 16a shows the mean and most probable $d\varepsilon/dx$ for 1/2" NaI. Since the most probable energy loss does significantly vary with ε, evaluation of an average most probable loss $\langle\Delta\varepsilon_p\rangle$ involved integration over the differential energy spectrum $dN/d\varepsilon$ for muons at sea level (Fig. 16b),[75] i.e.,

$$\langle\Delta\varepsilon_p\rangle = \int_{\varepsilon_{cutoff}}^{\infty} d\varepsilon\ \Delta\varepsilon_p(\varepsilon)\ \frac{dN}{d\varepsilon}(\varepsilon) \Big/ \int_{\varepsilon_{cutoff}}^{\infty} d\varepsilon\ \frac{dN}{d\varepsilon}(\varepsilon) = 5.63 \text{ MeV, where}$$

ε_{cutoff} = 250 MeV, and a power law drop in $dN/d\varepsilon$ at high ε makes the upper limit unimportant. This value for $\Delta\varepsilon_p$ gives $dL/d\varepsilon(\mu) = 0.365$ cal. sources/MeV, with an estimated error of ±3%.

Cross-calibration of the relativistic heavy ion data with other heavy ion data as described in Section II fixes the muon dL/dε datum point (■) as shown in Figs. 10 and 17. This relative efficiency is much higher than expected; it was anticipated that the muon point would fall on the electron efficiency (dL/dε) curves (dashed line[12] and Δ points[45,14]). The electron efficiency (dL/dε) curves are derived from either direct electron response or γ-ray response data,[14,12,13] in which the total energy ε of the electron or γ-ray (converted to an electron) produces a light signal L. These L/ε response curves, which are not constant (indicating a nonlinear response to electrons[76] and γ-rays[77]), are then used to generate a scintillation efficiency (dL/dε) curve which consequently shows a 30% variation in efficiency with dε/dx. Along with the efficiency curves in Fig. 17 is shown an electron response (L/ε) curve[12] (dash-dot); for this curve the ordinate axis gives L/ε (not dL/dε) and the abscissa axis gives the dε/dx corresponding to the initial energy ε of the electron. Similar interpretation of the figure axes holds for all γ-ray response (L/ε) data points.

To check whether the muon dL/dε and electron dL/dε do in fact coincide, an additional muon run was performed along with ^{137}Cs γ-ray (662 keV) and ^{241}Am γ-ray (59.5 keV) measurements. The results (hatched square and circles) show the γ-ray points fall (within errors) on the well-established electron response curve, with the muon point being about 2σ above its electron counterpart. These three points were normalized so as to place the ^{137}Cs γ-ray measurement on the electron response (L/ε) curve. Thus, the discrepancy between our two muon points is either due to the improper placement of the electron

efficiency relative to proton efficiency, to substantial errors resulting from our method of heavy ion data cross-calibration which placed the muon (■) point at its present position, to inaccuracies in the proton and alpha data[2,1] utilized in the cross-calibrations, or to a combination of the above.

Although the electron response (L/ε) and efficiency ($dL/d\varepsilon$) curves are well-established, their placement relative to proton $dL/d\varepsilon$ is not nearly so firm. We have searched the literature for information directly comparing electron response to proton efficiency, and have found conflicting data. Ophel[78] found L/ε for γ-rays in NaI to be 70% that of 5 MeV protons. However, he did not detect any non-linearity in γ-ray response with variation in γ-ray energy, contrary to other measurements.[77] Allison and Casson[4] measured ^{137}Cs γ-ray response in NaI compared to 60-400 keV protons, as shown in Fig. 17 (hatched triangle). The placement of this γ-ray datum point is predicated on the assumption that the scintillation efficiency of protons in NaI is constant for all energies. Should saturation occur for protons in NaI (not yet observed), the lower-energy proton points of Allison and Casson would be lowered with respect to maximum $dL/d\varepsilon$, thereby also bringing down the γ-ray point to values more consistent with present expectations. This would have a similar effect on the position of our muon point (■). Considering the fact that such proton saturation has been observed in CsI,[15] these might be considered strong arguments for the existence of proton saturation in NaI. (In addition, our scintillation model predicts proton saturation.)

Measurements in CsI[15] have also shown the electron and proton efficiency curves to join smoothly at $d\varepsilon/dx \approx 30 \frac{\text{MeV-cm}^2}{\text{g}}$, although

such direct data are lacking for NaI. One immediate question is whether protons (or other singly charged particles) at very low $d\varepsilon/dx$ exhibit the same decline in efficiency as do electrons. If the decline in electron efficiency with decrease in $d\varepsilon/dx$ is due to electron-hole recombination kinetics as discussed in Section III, then one expects the same decline to occur for protons. Unfortunately, no proton data exist to decide this issue. However, measurements of 61-222 MeV accelerator-produced pions and 245-5230 MeV accelerator-produced and cosmic ray muons in NaI have been made by Bowen[79] which fall in the interval of $d\varepsilon/dx$ where the electron efficiency curve is most steeply sloped. Bowen's intention was to test the accuracy of relativistic energy loss expressions which account for the density effect as well as energy straggling by directing the singly charged particles through a 1.51 cm thick NaI crystal and measuring the light output. Comparison of light output ΔL with predicted energy loss $\Delta\varepsilon$ for eleven energy values (four of which are shown in Fig. 17 giving the extremes in $d\varepsilon/dx$ for pions and muons) showed uniform agreement with theory to about 1%; the theoretical state of the art was considered sound. However, implicit in this treatment was the assumption of uniform scintillation efficiency, as indicated in Fig. 17. The particular absolute $dL/d\varepsilon$ value at which these points are placed is arbitrary; what is important is that for Bowen's conclusions to hold, they all must be at the same $dL/d\varepsilon$, with error bars that preclude any possibility of pions or muons having such a steeply sloped efficiency curve as exists for electrons. The only alternatives are to question the energy loss theory, since confirmed by additional experiments,[80] or to question Bowen's original measurement.

A future experiment is being planned with 0-60 MeV protons and a variety of γ-ray sources that may resolve some of the questions raised in this section, namely, does proton scintillation saturate at high $d\varepsilon/dx$, does proton efficiency drop at lower $d\varepsilon/dx$, and do the electron and proton efficiency curves meet and overlap?

Acknowledgements

We would like to thank Professor R. B. Murray for his very generous, warm, and informative discussions which occurred over the course of this work; they have substantially contributed to this paper. We also wish to thank Profs. M. Luntz, A. Portis, F. Reif, and Drs. C. J. Delbecq and R. G. Kaufman for helpful conversations. We thank Prof. P. B. Price for his continued support, and for his critical reading of the manuscript. We also thank the LBL Biomed research group for the kind use of their accelerator facilities.

This work was supported by the Director, Office of Energy Research, Division of Nuclear Physics of the Office of High Energy and Nuclear Physics, Division of the U.S. Department of Energy under Contract No. W-7405-ENG-48.

References

1. E. Newman and F.E. Steigert, Phys. Rev. 118, 1575 (1960).
2. F.S. Eby and W.K. Jentschke, Phys. Rev. 96, 911 (1954).
3. J.W. Blue and D.C. Liu, I.R.E. Trans. Nucl. Sci. 9, 48 (1962).
4. S.K. Allison and H. Casson, Phys. Rev. 90, 880 (1953).
5. M.R. Altman, H.B. Dietrich, R.B. Murray, and T.J. Rock, Phys. Rev. B 7, 1743 (1973).
6. R.W. Birkmire, R.B. Murray, and M. Luntz, Phys. Rev. B 15, 31 (1977).
7. J.C.D. Milton and J.S. Fraser, Phys. Rev. 96, 1508 (1954).
8. E.N. Shipley, G.E. Owen, and L. Madansky, Rev. Sci. Instr. 30, 604 (1959).
9. R.H. Lovberg, Phys. Rev. 84, 852 (1951).
10. E.A. Womack, A.J. Lazarus, and S.W.W. Liu, Phys. Rev. 144, 231 (1966).
11. A. Meyer and R.B. Murray, Phys. Rev. 128, 98 (1962).
12. J.R. Prescott and G.H. Narayan, Nucl. Instr. Meth. 75, 51 (1969).
13. A.J.L. Collinson and R. Hill, Proc. Phys. Soc. 81, 883 (1963).
14. C.D. Zerby, A. Meyer, and R.B. Murray, ORNL-3016; also in Nucl. Instr. Meth. 12, 115 (1961).
15. R. Gwin and R.B. Murray, Phys. Rev. 131, 501 (1963).
16. J.B. Schutt, J.F. Arens, C.M. Shai, and E. Stromberg, Appl. Optics 13, 2218 (1974).
17. S.P. Ahlen, B.G. Cartwright, and G. Tarlé, Nucl. Instr. Meth. 143, 513 (1977).
18. M.H. Salamon and G. Tarlé, Nucl. Instr. Meth. 161, 147 (1979).
19. M.H. Salamon, Lawrence Berkeley Laboratory Report No. 10446 (1980).

20. S.P. Ahlen, Rev. Mod. Phys. 52, 121 (1980).

21. M.H. Salamon, S.P. Ahlen, G. Tarlé, and K.C. Crebbin, Phys. Rev. A, in press.

22. RCA Photomultiplier Manual, Technical Senes PT-61 (1970).

23. J.R. Prescott, Nucl. Instr. Meth. 39, 173 (1966).

24. M. Garbury, T.P. Vogl, J.R. Hansen, Rev. Sci. Instr. 28, 826 (1957)

25. A.R. Quinton, C.E. Anderson, and W.J. Knox, Phys. Rev. 115, 886 (1959).

26. M. Luntz, private communication.

27. U. Fano and W. Lichten, Phys. Rev. Lett. 14, 627 (1965); Inter. Conf. on the Physics of Electronic and Atomic Collisions, 7th, Amsterdam, 1971.

28. J.B. Birks, The Theory and Practice of Scintillation Counting, Pergamon, New York, 1964.

29. R.G. Kaufman, W.B. Hadley, and H.N. Hersh, IEEE Trans. Nucl. Sci. 17, 82 (1970).

30. R.B. Murray, IEEE Trans. Nucl. Sci. 22, 54 (1975).

31. H.B. Dietrich, A.E. Purdy, R.B. Murray, and R.T. Williams, Phys. Rev. B 8, 5894 (1973).

32. W.B. Hadley, S. Polick, R.G. Kaufman, and H.N. Hersh, J. Chem. Phys. 45, 2040 (1966).

33. R.T. Williams, J.N. Bradford, and W.L. Faust, Phys. Rev. B 18, 7038 (1978).

34. T.G. Castner and W. Känzig, J. Phys. Chem. Sol. 3, 178 (1957).

35. R.D. Popp and R.B. Murray, J. Phys. Chem. Sol. 33, 601 (1972).

36. E.g., F.K. Fong, ed., Radiationless Processes in Molecules and Condensed Phases, Springer-Verlag, 1976.

37. W.J. Van Sciver and L. Bogart, I.R.E. Trans. Nucl. Sci. NS-3, No. 3, 90 (1958).

38. C.J. Delbecq, A.K. Ghosh, and P.H. Yuster, Phys. Rev. 151, 599 (1966).

39. Refs. 32 and 31 attribute "prompt" trapping to holes being formed within the reaction sphere of a Tl ion, resulting in immediate capture. This has led to estimates of Tl reaction radius which we believe are erroneous. A computer kinetics model, not described in this paper, demonstrates that free hole diffusion prior to self-trapping is sufficient to account for the observed prompt trapping fractions, with a reaction radius as small as 3-4 Å.

40. C.J. Delbecq, Y. Toyozawa, and P.H. Yuster, Phys. Rev. B 9, 4497 (1974).

41. H.B. Dietrich and R.B. Murray, J. Lumin. 5, 155 (1972).

42. I.K. Pliavin',Opt. Spectrosc. 7, 41 (1959).

43. R.G. Kaufman and W.B. Hadley, J. Chem. Phys. 47, 264 (1967).

44. E.D. Aluker and D.J. Lusis, Phys. Stat. Sol. A19, 759 (1973).

45. R.B. Murray and A. Meyer, Phys. Rev. 122, 815 (1961).

46. R. Katz and E.J. Kobetich, Phys. Rev. 170, 397 (1968).

47. M. Ladu, M. Pellicioni, and M. Roccella, Nucl. Instr. Meth. 101, 383 (1972).

48. J.B. Birks, IEEE Trans. Nucl. Sci. NS-11, 4 (1964).

49. R. Voltz, J. Lopes da Silva, G. Laustriat, and A. Coche, J. Chem. Phys. 45, 3306 (1966).

50. M. Luntz, Phys. Rev. B 4, 2857 (1971).

51. M.N. Kabler and R.T. Williams, Phys. Rev. B 18, 1948 (1978).

52. R.B. Murray, private communication.

53. J.A. Harshaw, H.C. Kremers, E.C. Stewart, E.K. Warburton, and J.O. Hay, U.S.A.E.C. Report NYO-1577 (1952), unpublished. See ref. 45 for display of this data.

54. P.D. Johnson and F.E. Williams, J. Chem. Phys. 18, 1477 (1950).

55. L. Apker and E. Taft, Phys. Rev. 81, 698 (1951).

56. H. Nishimura and M. Tomura, J. Phys. Soc. Jap. 39, 390 (1975).

57. E. Strauss, W.J. Maniscalco, W.M. Yen, U.C. Kellner, and V. Gerhardt, Phys. Rev. Lett. 44, 824 (1980).

58. G. Paillotin, C.E. Stromberg, J. Breton, and N.E. Geacintov, Biophysical J. 25, 513 (1979).

59. Y. Toyozawa, J. Phys. Soc. Jap. 44, 482 (1978).

60. K. Tanimura and T. Okada, Phys. Rev. B 21, 1690 (1980).

61. E.J. Kobetich and R. Katz, Phys. Rev. 170, 391 (1968).

62. J. Faïn, M. Monnin, and M. Montret, Rad. Res. 57, 379 (1974).

63. A. Chatterjee, H. Maccabee, and C.A. Tobias, Rad. Res. 54, 479 (1973).

64. R.M. Sternheimer, Phys. Rev. 164, 349 (1967).

65. L. Katz and A.S. Penfold, Rev. Mod. Phys. 24, 28 (1952).

66. M.J. Berger and S.M. Seltzer, NAS-NRC Publication 1133 (1964).

67. B.N.S. Rao, Nucl. Instr. Meth. 44, 155 (1966).

68. N. Bohr, Phil. Mag. 25, 10 (1913); Phil. Mag. 30, 581 (1915).

69. J.D. Jackson, Classical Electrodynamics, Wiley, 1962.

70. E. Merzbacher and H.W. Lewis, Encyclopedia of Physics 34/2, Springer-Verlag, p. 166, 1968.

71. See, e.g., E.H.S. Burhop, The Auger Effect and Other Radiationless Transitions, Cambridge University Press, 1952.

72. G.D. Byrne and A.C. Hindemarsh, ACM Trans. Math. Software 1, 71 (1975); UCID-30112, Rev. 1.

73. L. Landau, J. Phys. USSR 8, 201 (1944).

74. B. Rossi, High-Energy Particles, Prentice-Hall, 1952.

75. Y. Pal and B. Peters, Kgl. Danske Videnskab. Selskab. Mat.-Fys. Medd. 33, No. 15 (1964).

76. F.T. Porter, M.S. Freedman, F. Wagner, and I.S. Sherman, Nucl. Instr. Meth. 39, 754 (1954).

77. D. Engelkeimer, Rev. Sci. Instr. 27, 589 (1956).

78. T.R. Ophel, Nucl. Instr. 3, 49 (1958).

79. T. Bowen, Phys. Rev. 96, 754 (1954).

80. E.H. Bellemy, R. Hofstadter, W.L. Lakin, J. Cox, M.L. Perl, W.T. Toner, and T.F. Zipf, Phys. Rev. 164, 417 (1967).

81. G.M. Tisljar-Lentulis, Rev. Sci. Instr. 37, 291 (1966).

82. J.G. Likely and W. Franzen, Phys. Rev. 87, 666 (1952).

83. G. Mechtersheimer, G. Büche, U. Klein, W. Kluge, H. Matthäy, and D. Münchmeyer, Nucl. Phys. A324, 379 (1979).

84. W. Schött and A. Flammersfeld, Z. Naturforschg. 21a, 1075 (1966).

Table Captions

Table 1. PMT response to light pulse train from the rotating mirror assembly. In each of the four pulse trains shown, all signals are given relative to highest amplitude in each train (pulse #8). The first pair of pulse trains compares unattenuated to $10^{0.4}$ attenuated signals. No saturation is observed over this high intensity region where light intensity varies by a factor of 15. The second pair compares unattenuated to 10^{2} attenuated signals. Five of the eight pulse peaks in the 2.0 filter group were obscured due to spectrum overlap accompanying the larger FWHM associated with these light levels. The three remaining pulses, however, are enough to confirm linear response. We note that the pulse #1 deviation is not only almost within errors, but is in the opposite direction expected for saturation.

Table 2. Shell parameters. For each principal atomic shell in the NaI molecule the average ionization potential I_i, oscillator strength f_i ($\sum_i f_i = 1$), and Ω_i are listed. Ω_i is the fraction of shell ionization energy not transported away from the molecule by Auger or fluorescence processes.

Table 1

Filter density	1	2	3	4
0.4	0.164 ± 0.002	0.291 ± 0.002	0.347 ± 0.002	0.399 ± 0.002
0.0	0.167 ± 0.001	0.291 ± 0.001	0.349 ± 0.001	0.395 ± 0.001
	5	6	7	8
2.0	0.597 ± 0.002	0.787 ± 0.002	0.828 ± 0.002	1.000
0.0	0.597 ± 0.001	0.787 ± 0.001	0.828 ± 0.001	1.000
	1	2	3	4
2.0	0.180 ± 0.013	-	-	-
0.0	0.164 ± 0.001	-	-	-
	5	6	7	8
2.0	0.598 ± 0.010	-	-	1.000
0.0	0.606 ± 0.001	-	-	1.000

Table 2

Shell	I_i (keV)	f_i	Ω_i
Na, K	1.07	2/64	0.10
Na, L	0.054	8/64	1.0
Na, M	0.005	1/64	1.0
I, K	33.2	2/64	0.023
I, L	4.79	8/64	0.08
I, M	0.766	18/64	0.24
I, N	0.091	18/64	1.0
I, O	0.027	7/64	1.0

Figure Captions

Figure 1. Experimental configuration for Bevalac heavy ion exposures.

Figure 2. "Raw" light response curves for ^{20}Ne (a), ^{40}Ar (b), and ^{56}Fe (c). Ordinate values are proportional to measured signals, and abscissa values are calculated using the fitting method described in text. Excellent agreement between data (●) and fit (○) is evident.

Figure 3. $L(\varepsilon)$ polynomial curves for ^{20}Ne, ^{40}Ar, and ^{56}Fe.

Figure 4. Scintillation efficiency curves ($dL/d\varepsilon$ vs $d\varepsilon/dx$) for both relativistic heavy ion data and low energy heavy ion data.[1] The error bars on the low energy data represent uncertainties in the cross-calibration procedure. Error bars on relativistic ion data represent experimental errors.

Figure 5. a) $dL/d\varepsilon$ calculated from $L(E)$ for NE110, a commercial plastic scintillator, where $L(E)$ is a fitted polynomial of order $n = 3$ to 7. Insensitivity to polynomial order is demonstrated for $50 < E < 500$ MeV/amu.

b) Least squares χ^2 vs polynomial order n, from which $n = 5$ was chosen as optimal. The anomalous increase in χ^2 at $n = 6$ is most likely due to onset of computational ill-condition.

Figure 6. a-c) Linear tube response is shown for three separate voltage levels. Error bars represent estimates of FWHM measurement errors which are obviously overestimated.

d) Baffle out/baffle in signal ratio as function of total light intensity.

Figure 7. Rotating mirror assembly used in test of PMT linearity.

Figure 8. Scintillation efficiency $dL/d\varepsilon$ of relativistic ^{20}Ne, ^{40}Ar, and ^{56}Fe as function of energy E (MeV/amu).

Figure 9. Total light output L vs $\in = K^3 A \beta_0{}^3/Z^{2/3}$, where Z,A = ion atomic number and weight (in amu), β_0 is the entering velocity of the ion (in units of c), and K is the constant $(\frac{1}{2} m_\mu c^2)^{\frac{1}{2}}$, $m_\mu = 931.5$ MeV/c^2. The NS data falls within the band as shown.

Figure 10. Collected NaI:Tl scintillation efficiency ($dL/d\varepsilon$) data vs stopping ($d\varepsilon/dx$) for various particles. The upper left segment of the figure is expanded in Fig. 17 for increased clarity. Sources of these data are: ref. 1, low energy heavy ion curves (solid lines), alphas (▲); ref. 2, protons (○) and alphas (●); ref. 4, protons (open square with plus sign) and γ-rays (hatched open triangle); ref. 15, proton response in CsI:Tl (long dash-short dash curve). The remaining data is referenced in the caption of Fig. 17.

Figure 11. A fit of $dL/d\varepsilon \propto 1 - n(0)/[1+K_2 n(0)\tau]$, (circles), to electron efficiency curve (line). n(0) is taken to be proportional to $d\varepsilon/dx$, and the resulting points are normalized along the (arbitrary scale) $dL/d\varepsilon$ direction by a factor of 1.04 to optimize the fit.

Figure 12. Typical dose profile calculated by model for Z = 26, E = 500 MeV/amu. Both axes are logarithmic, dose units in the figure being keV/cm-Å^2. The small peak at $\approx 10^6$ Å is due to absorption of iodine K-shell X-rays at the

photon absorption length. The general graininess in the "halo" region (where dose is due to δ-ray slowing) is an artifact of the finite sized annuli.

Figure 13. Comparison of scintillation model with collected experimental data. Dashed lines give proton and alpha data of ref. 2, the heavy ion data of NS (ref. 1), and our relativistic heavy ion data. Triangles (▲) mark scintillation efficiencies calculated by the model; solid lines are drawn between them for ease of visualization only and are not to convey additional information.

Figure 14. Experimental configuration used in measurement of cosmic-ray muon scintillation efficiency.

Figure 15. Muon energy loss spectrum in the NaI:Tl crystal, after appropriate binning of pulse height analyzer (PHA) channels. The open square (□) with error bars indicates peak position estimate.

Figure 16. a) Differential energy spectrum of cosmic-ray muons at sea level. This figure appears in ref. 75 and is directly borrowed from that paper.

b) Mean ($\bar{\Delta}$) and most probable (Δ_p) energy loss for muons in 1/2" thick NaI as function of energy ε. Division by the crystal thickness X as shown in the figure gives these values as stopping powers.

Figure 17. Collected scintillation efficiency (dL/dε) data for various particles at low dε/dx. See text for special interpretation of the axes for γ-rays and the electron response (L/ε) curve. Sources of these data are: ref. 79, high

energy pions (◆) and muons (◇); ref. 4, ^{137}Cs γ-rays (hatched triangle); ref. 12, electron efficiency ($dL/d\varepsilon$) curve (dashed line) and electron response (L/ε) curve (dash-dot line); ref. 78, γ-rays (▼), where the γ-ray point within parentheses was measured in LiI(Eu), not NaI:Tl; ref. 2 protons (○); ref. 81 (additional references therein) protons (□ and ▽); ref. 82, protons (open square enclosing multiplication sign); ref. 83, protons (⊗); ref. 84, electrons (⊕); this work, muons (■ and hatched open square, and γ-rays (hatched open circle).

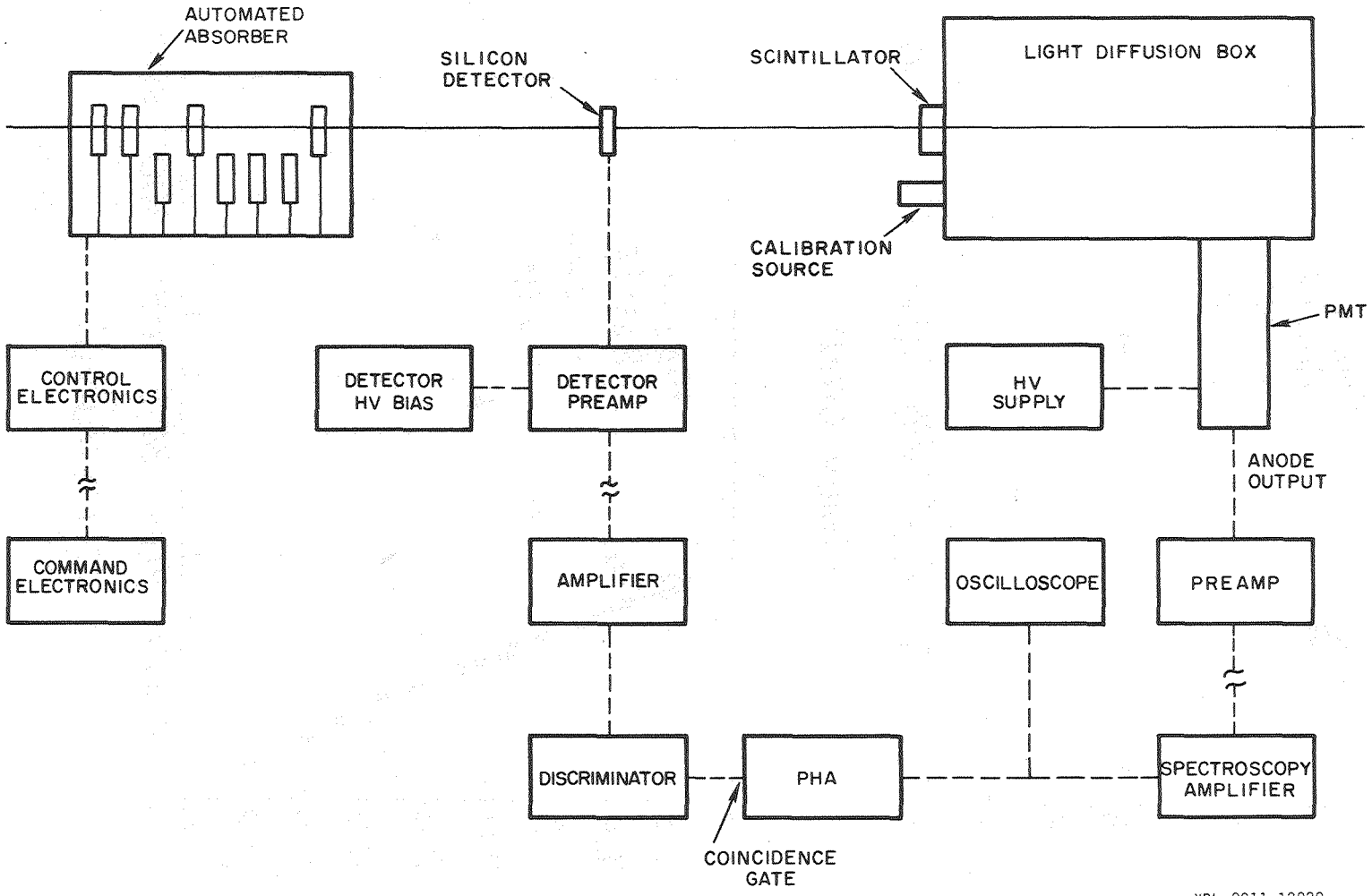
AUTOMATED ABSORBER
SILICON DETECTOR
SCINTILLATOR
LIGHT DIFFUSION BOX
CALIBRATION SOURCE
PMT
CONTROL ELECTRONICS
DETECTOR HV BIAS
DETECTOR PREAMP
HV SUPPLY
ANODE OUTPUT
COMMAND ELECTRONICS
AMPLIFIER
OSCILLOSCOPE
PREAMP
DISCRIMINATOR
PHA
SPECTROSCOPY AMPLIFIER
COINCIDENCE GATE
XBL 8011-12820

Figure 1

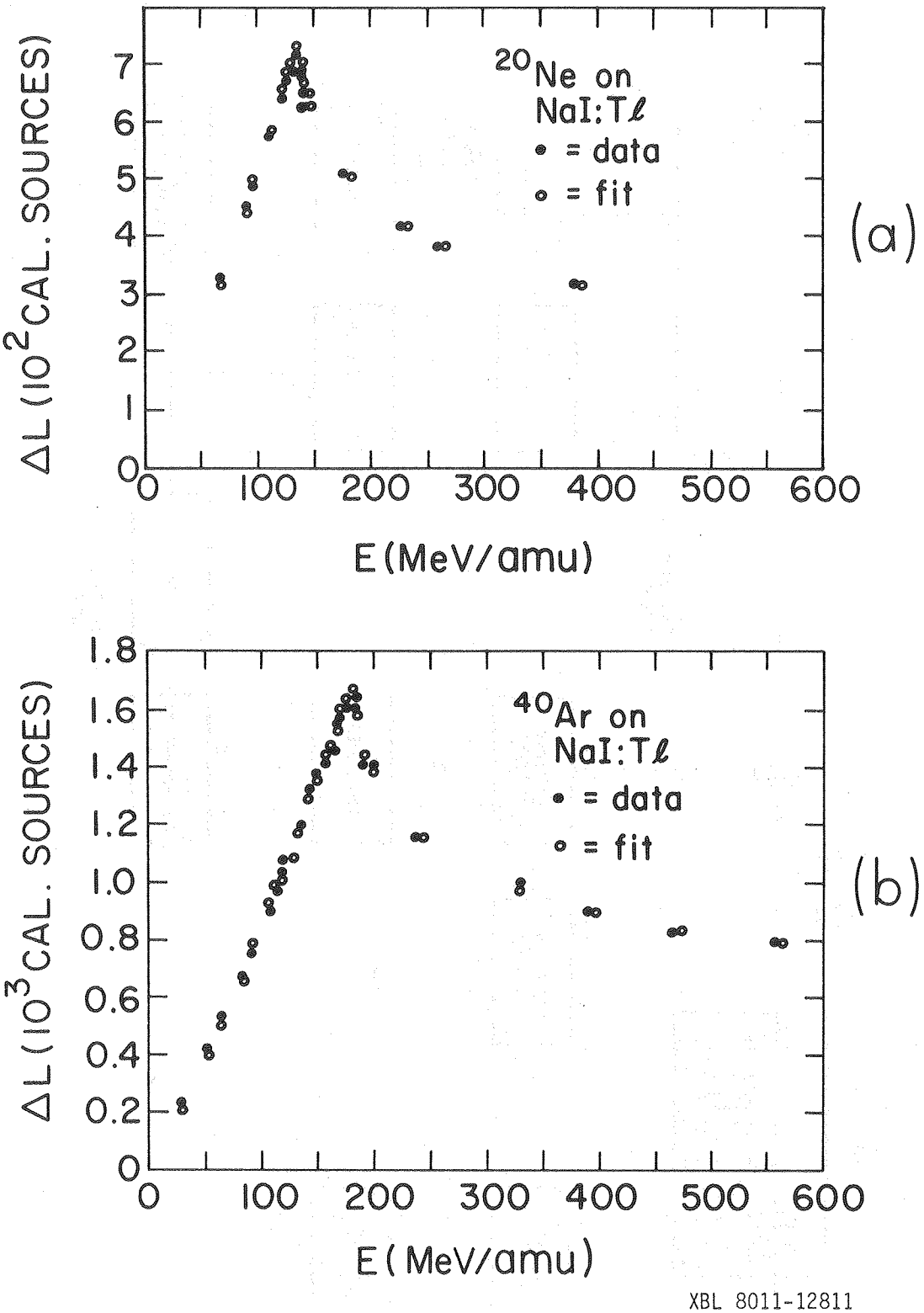
ΔL (10² CAL. SOURCES)
²⁰Ne on NaI:Tℓ
• = data
○ = fit
(a)
E (MeV/amu)
ΔL (10³ CAL. SOURCES)
⁴⁰Ar on NaI:Tℓ
• = data
○ = fit
(b)
E (MeV/amu)
XBL 8011-12811

Figure 2a,b

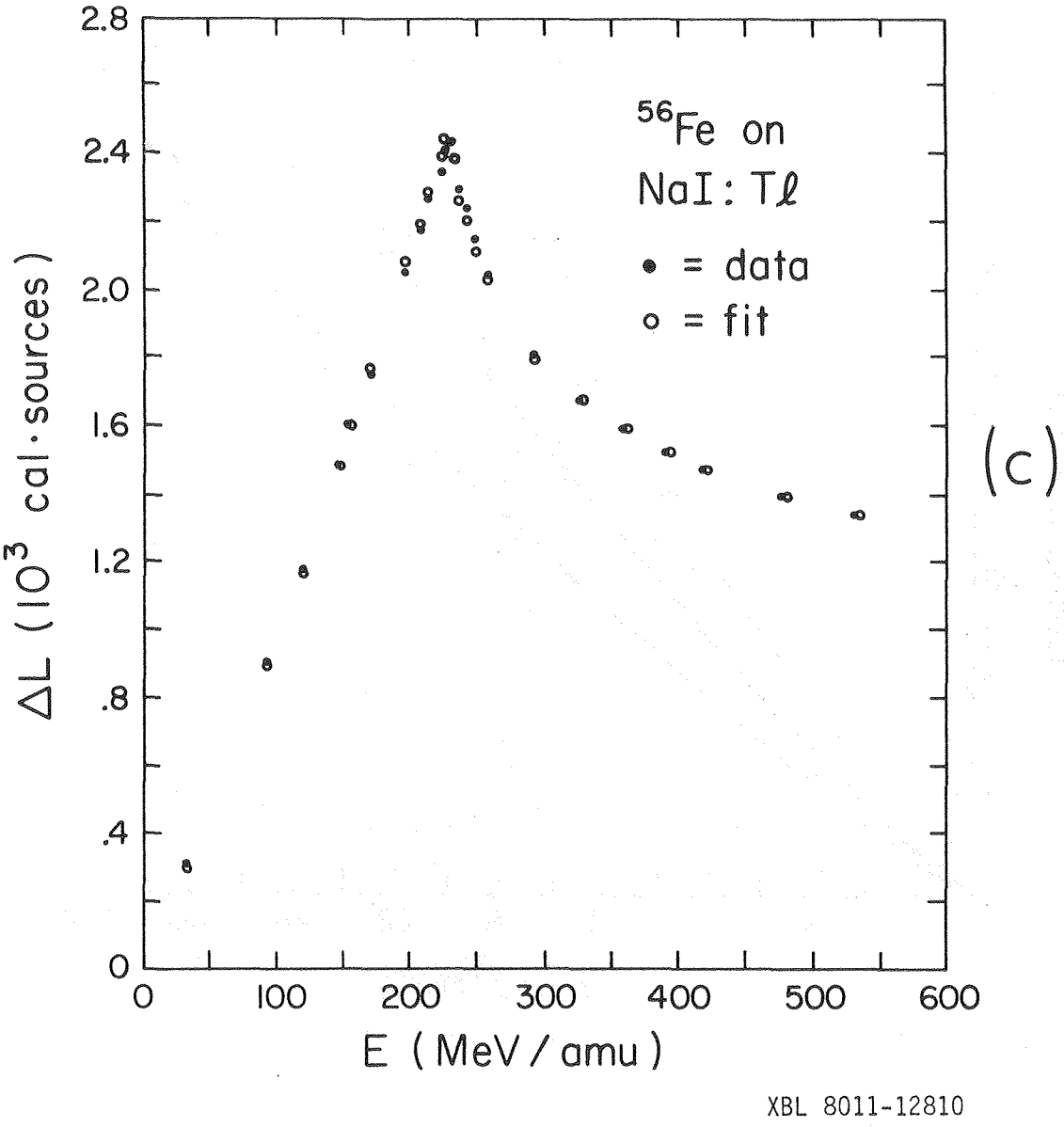
2.8
2.4
2.0
1.6
1.2
.8
.4
0
ΔL (10^3 cal · sources)
0
100
200
300
400
500
600
E (MeV / amu)
^{56}Fe on
NaI : Tℓ
• = data
o = fit
(c)
XBL 8011-12810

Figure 2c

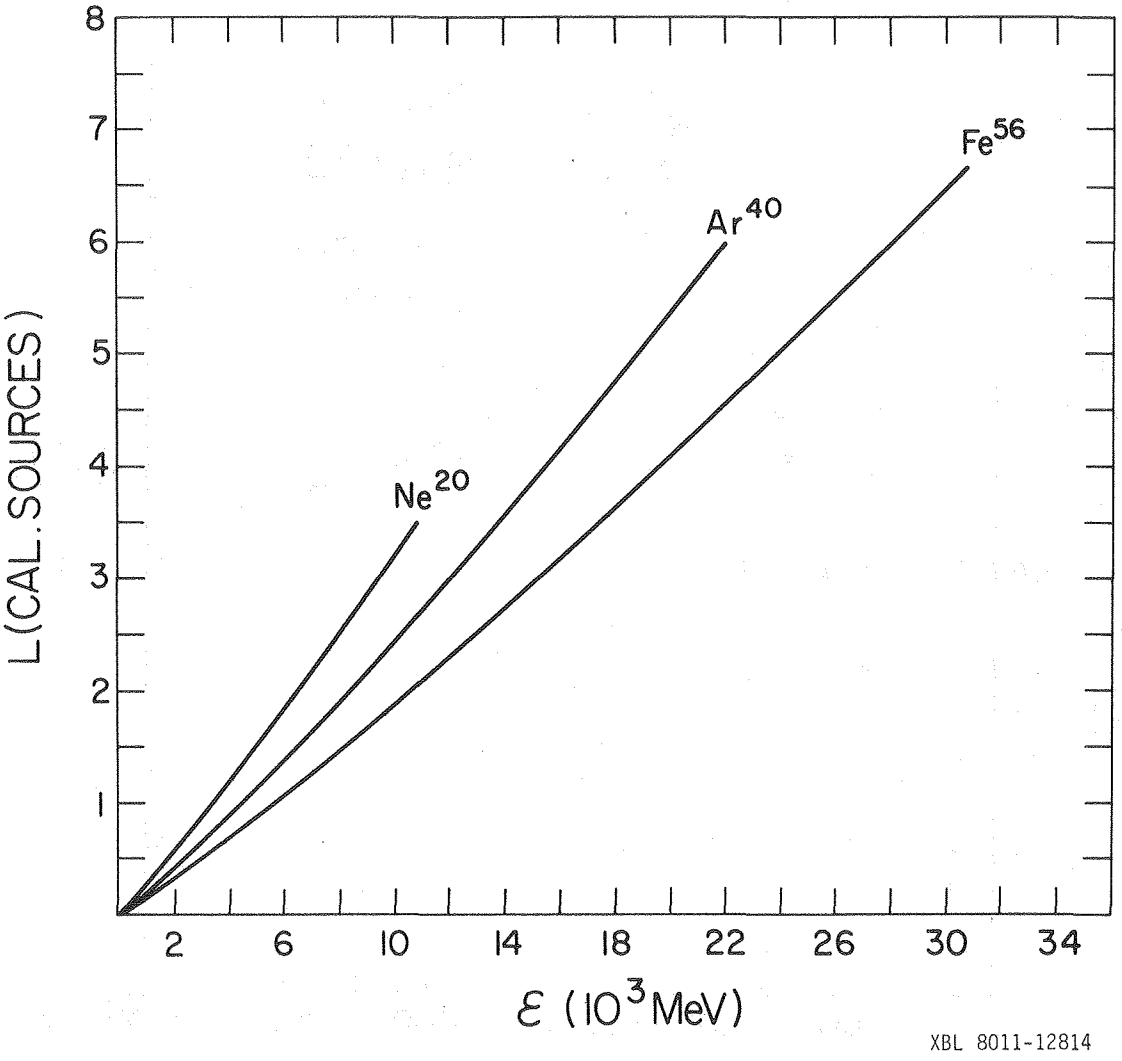
L(CAL. SOURCES)
8
7
6
5
4
3
2
1
Fe56
Ar40
Ne20
2
6
10
14
18
22
26
30
34
ε (10³MeV)
XBL 8011-12814

Figure 3

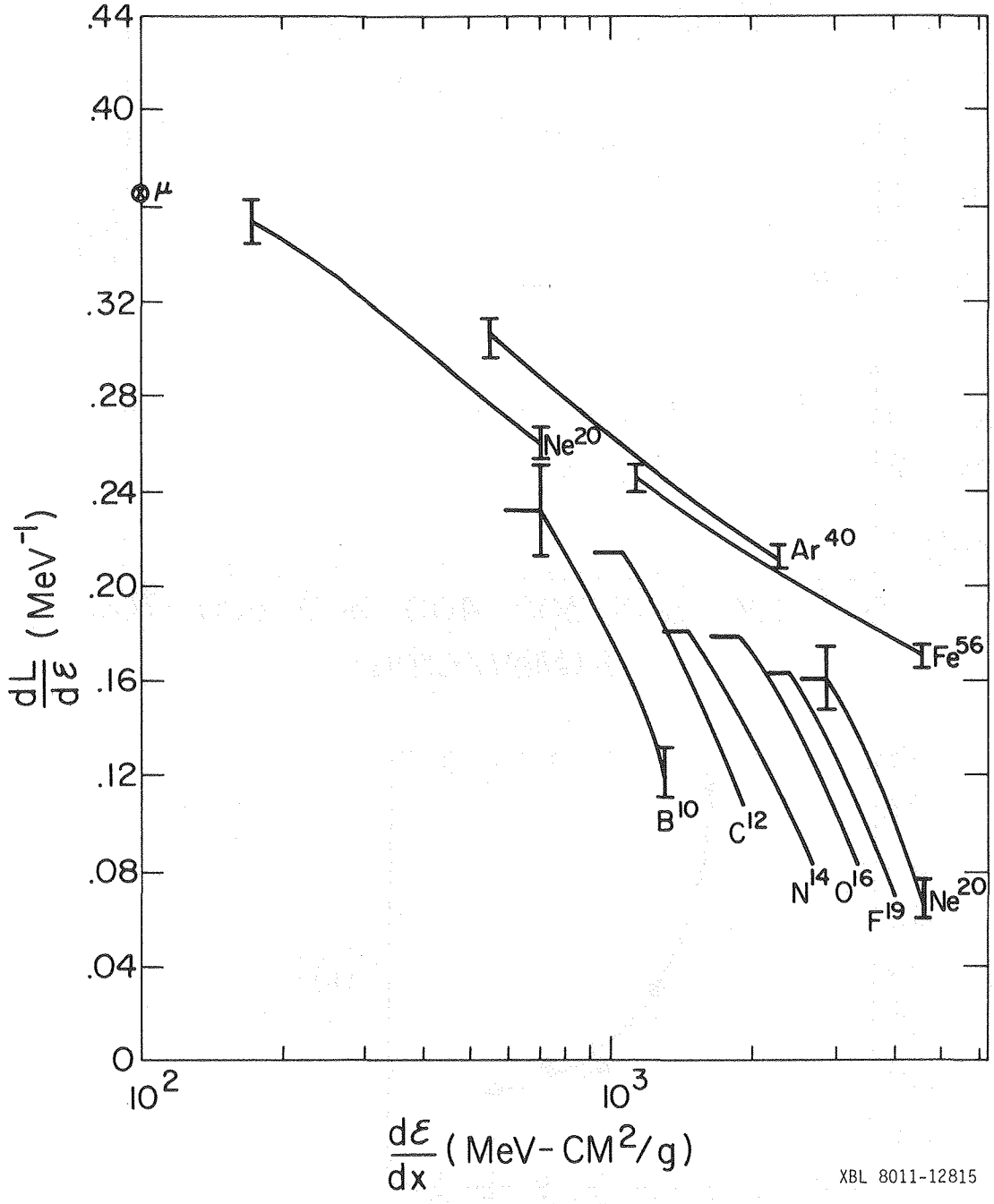
.44
.40
⊗μ
.32
.28
.24
.20
.16
.12
.08
.04
0
10^2
10^3
$\frac{dL}{d\varepsilon}$ (MeV^{-1})
$\frac{d\varepsilon}{dx}$ (MeV-CM^2/g)
Ne^{20}
Ar^{40}
Fe^{56}
B^{10}
C^{12}
N^{14}
O^{16}
F^{19}
Ne^{20}
XBL 8011-12815

Figure 4

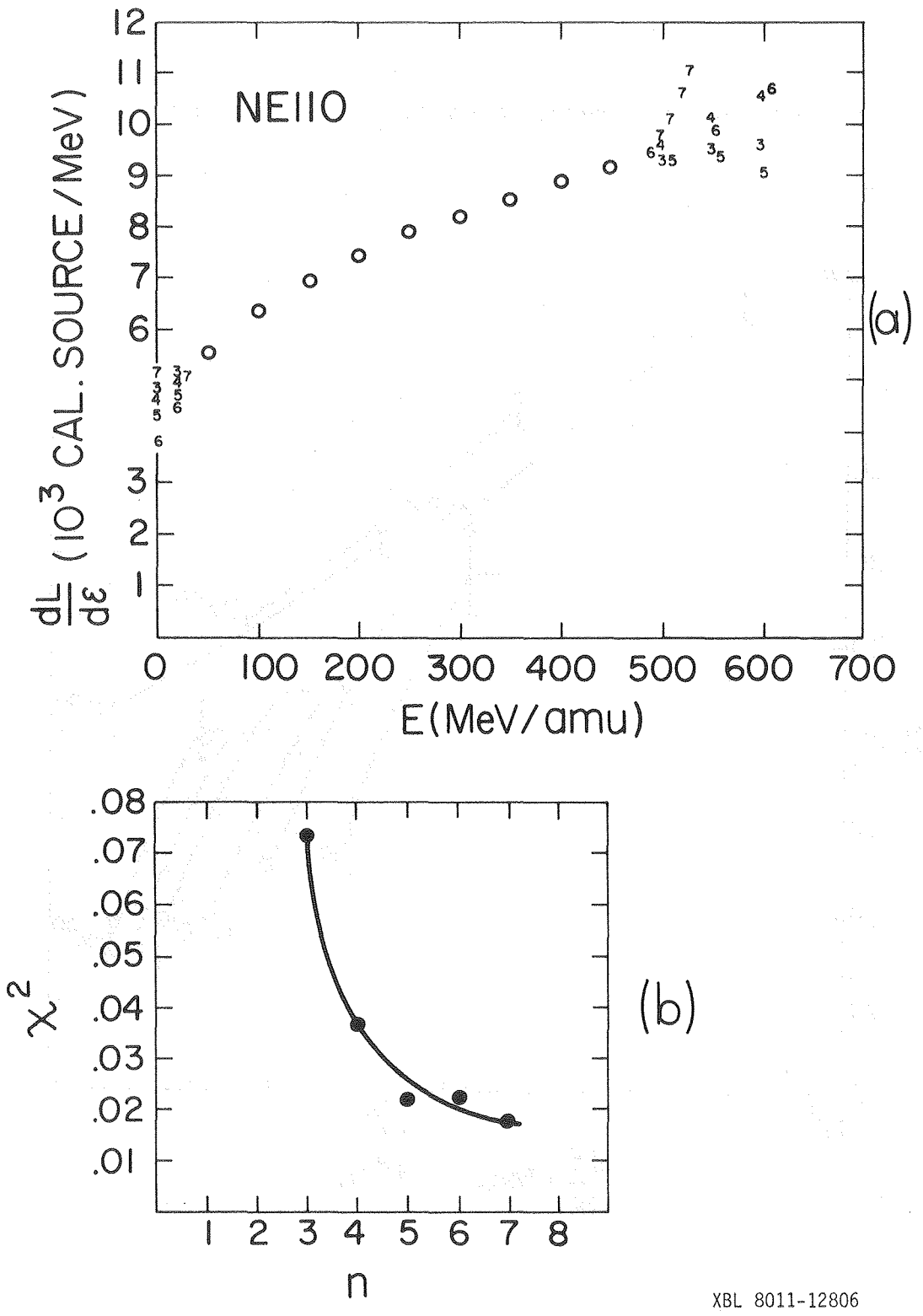
NE110
$\frac{dL}{d\varepsilon}$ (10^3 CAL. SOURCE/MeV)
E(MeV/amu)
(a)
χ^2
n
(b)
XBL 8011-12806

Figure 5a,b

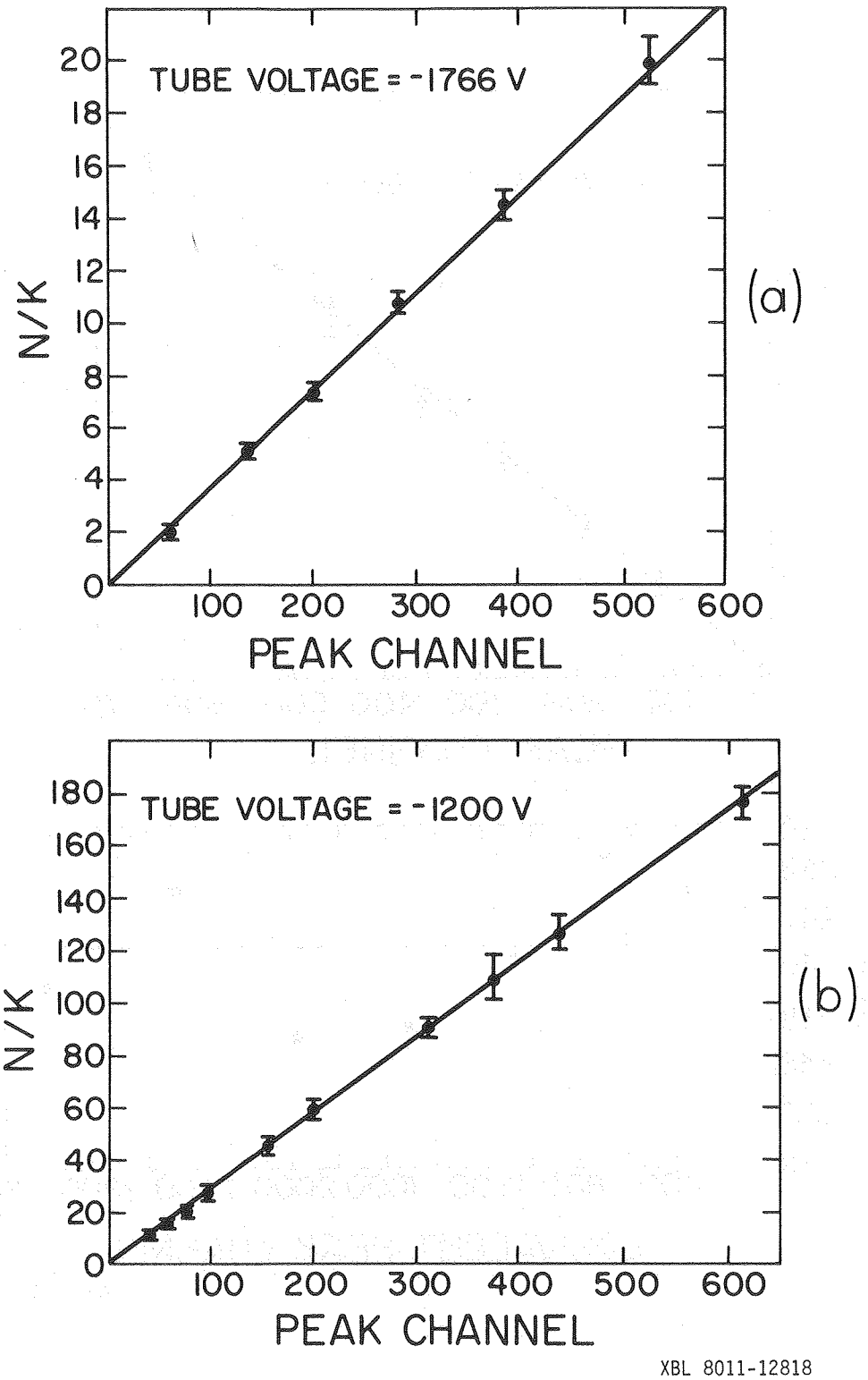
TUBE VOLTAGE = -1766 V
N/K
PEAK CHANNEL
(a)
TUBE VOLTAGE = -1200 V
N/K
PEAK CHANNEL
(b)
XBL 8011-12818

Figure 6a,b

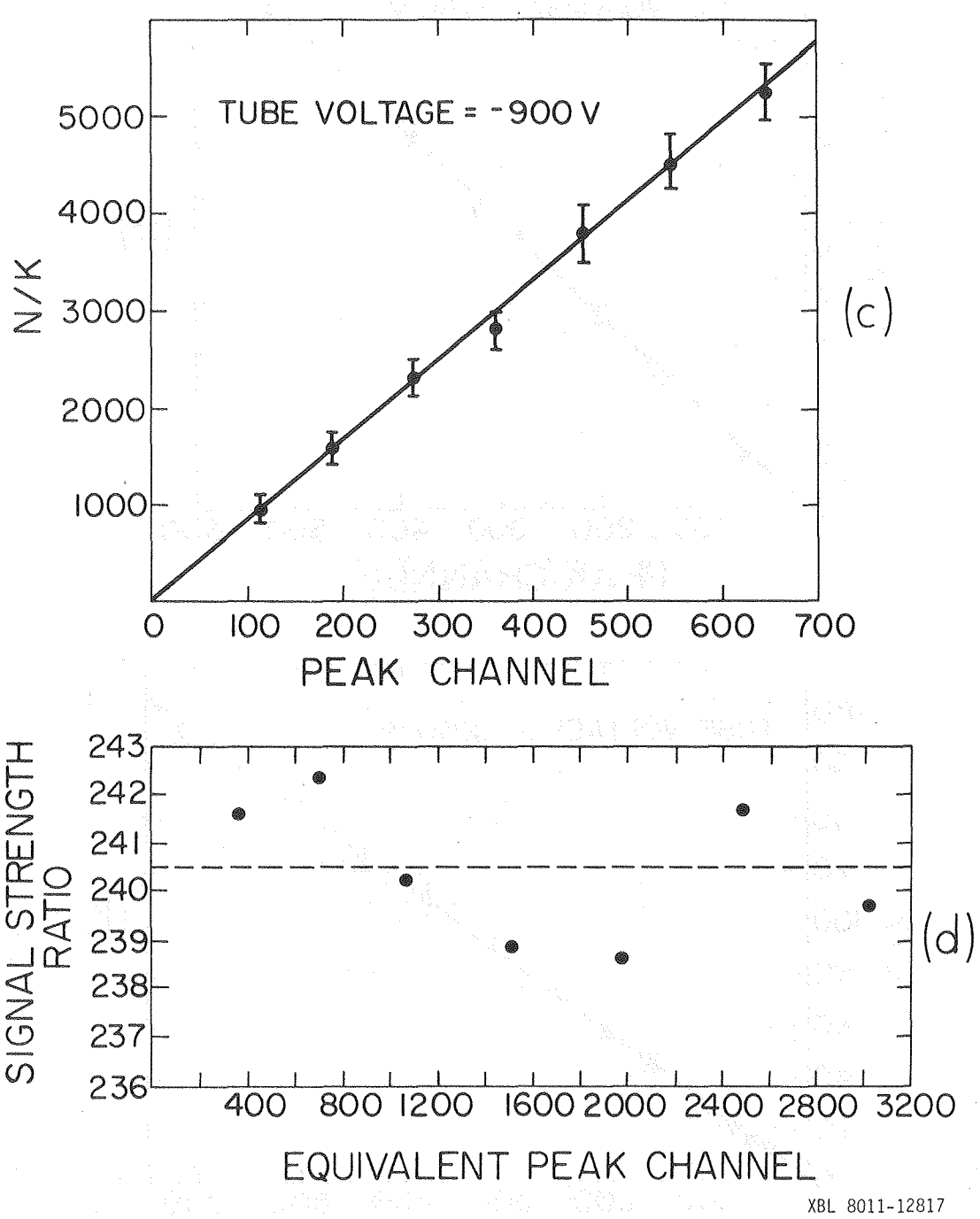
TUBE VOLTAGE = -900 V
N/K
5000
4000
3000
2000
1000
0
100
200
300
400
500
600
700
PEAK CHANNEL
(c)
SIGNAL STRENGTH RATIO
243
242
241
240
239
238
237
236
400
800
1200
1600
2000
2400
2800
3200
EQUIVALENT PEAK CHANNEL
(d)
XBL 8011-12817

Figure 6c,d

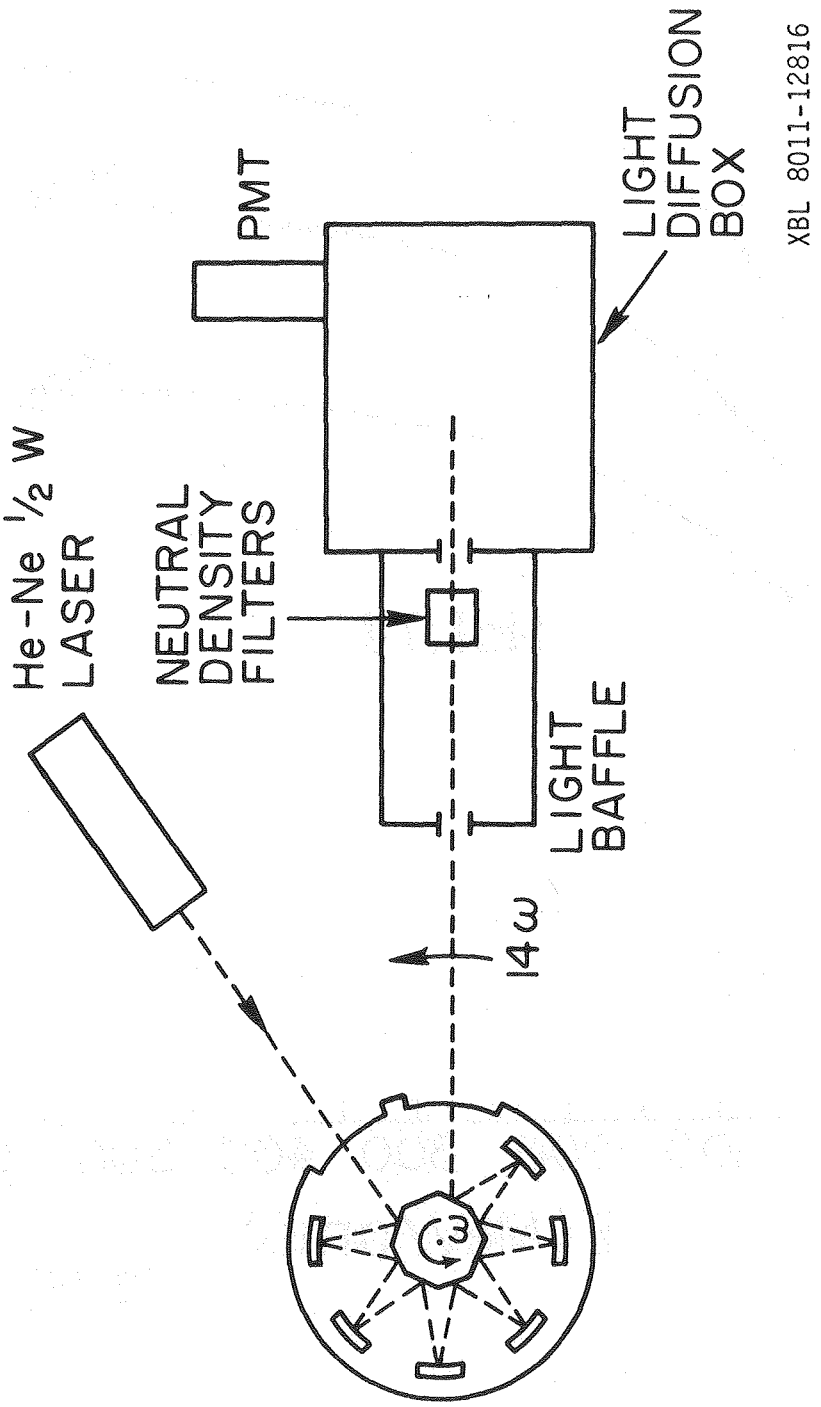
He-Ne ½ W
LASER
NEUTRAL
DENSITY
FILTERS
PMT
LIGHT
DIFFUSION
BOX
LIGHT
BAFFLE
14 ω
XBL 8011-12816

Figure 7

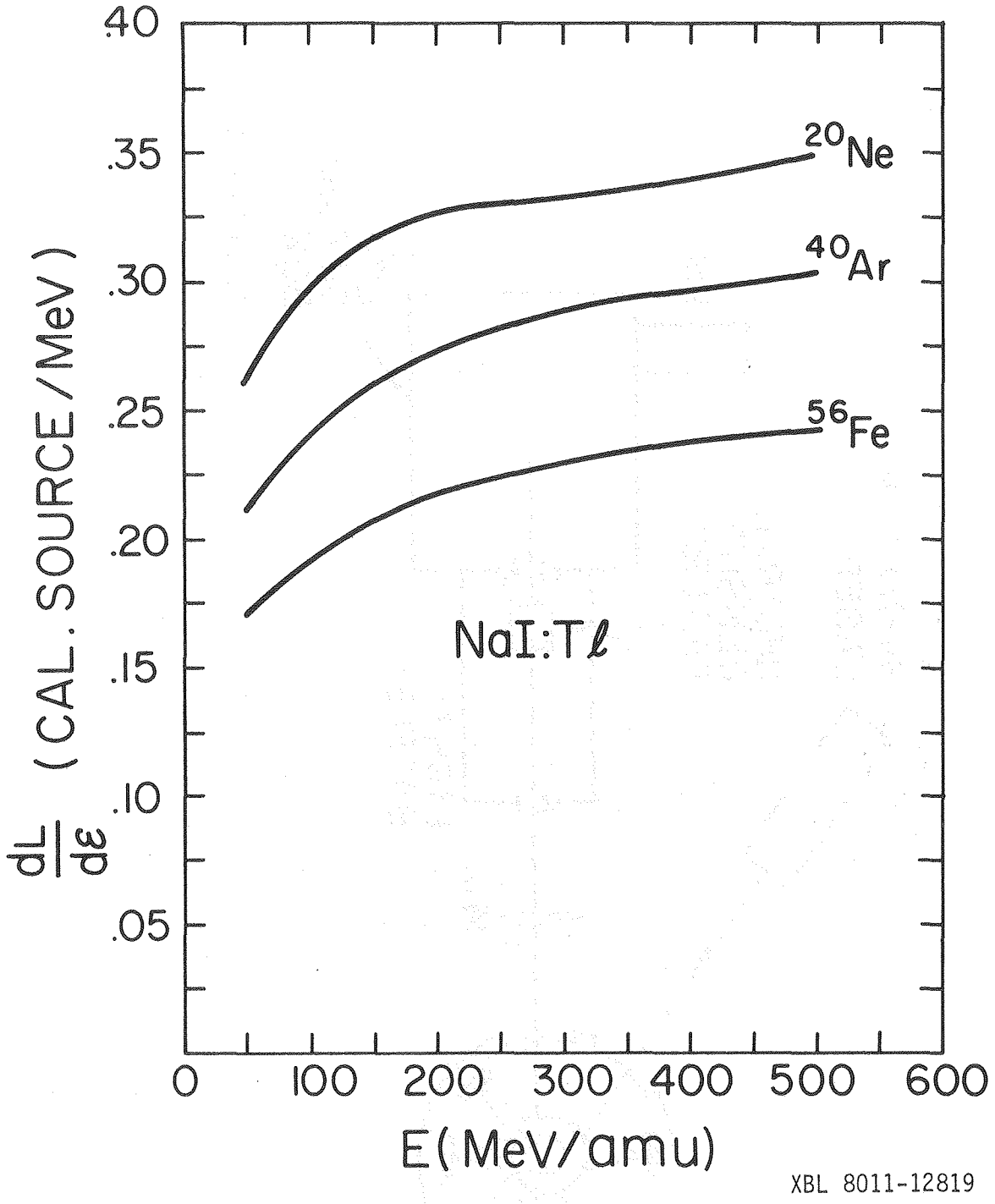
.40
.35
.30
.25
.20
.15
.10
.05
$\frac{dL}{d\varepsilon}$ (CAL. SOURCE/MeV)
^{20}Ne
^{40}Ar
^{56}Fe
NaI:Tℓ
0
100
200
300
400
500
600
E(MeV/amu)
XBL 8011-12819

Figure 8

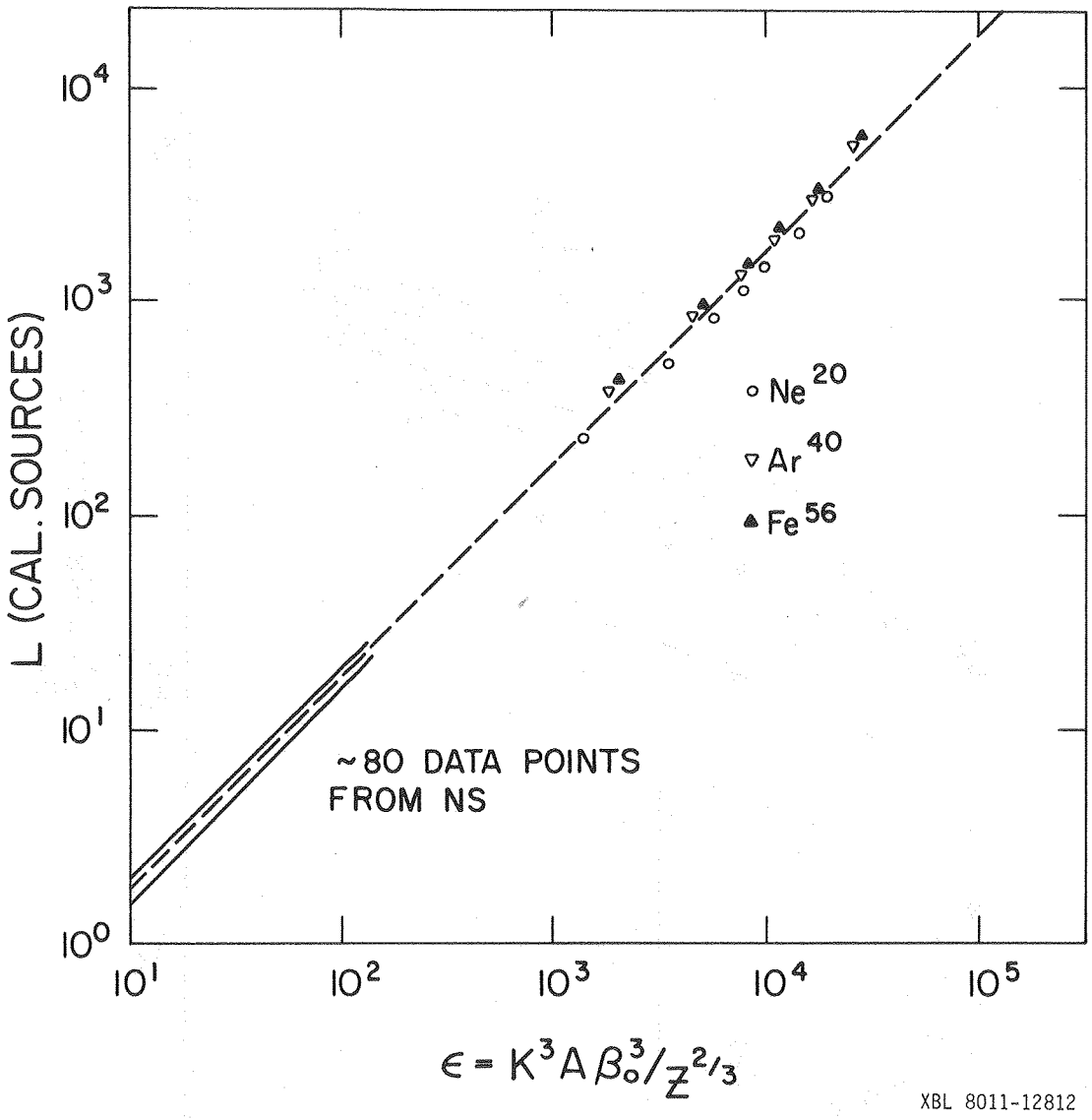
L (CAL. SOURCES)
10^4
10^3
10^2
10^1
10^0
10^1
10^2
10^3
10^4
10^5
○ Ne^{20}
▽ Ar^{40}
▲ Fe^{56}
~80 DATA POINTS
FROM NS
$\epsilon = K^3 A \beta_o^3 / Z^{2/3}$
XBL 8011-12812

Figure 9

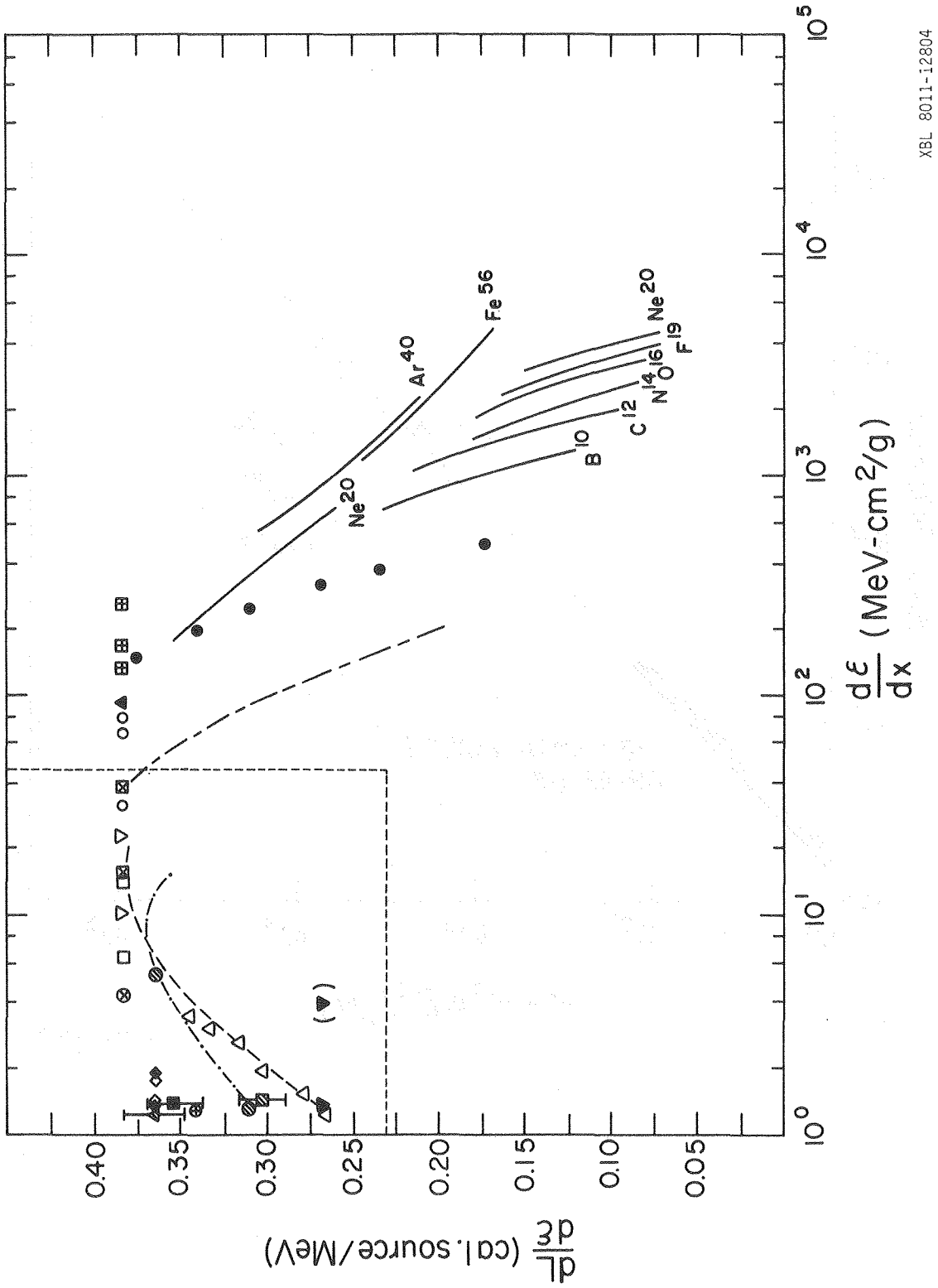
$\frac{dL}{d\varepsilon}$ (cal. source/MeV)
0.40
0.35
0.30
0.25
0.20
0.15
0.10
0.05
10^0
10^1
10^2
10^3
10^4
10^5
$\frac{d\varepsilon}{dx}$ (MeV-cm^2/g)
Ne^{20}
Ar^{40}
Fe^{56}
B^{10}
C^{12}
N^{14}
O^{16}
F^{19}
Ne^{20}
XBL 8011-12804

Figure 10

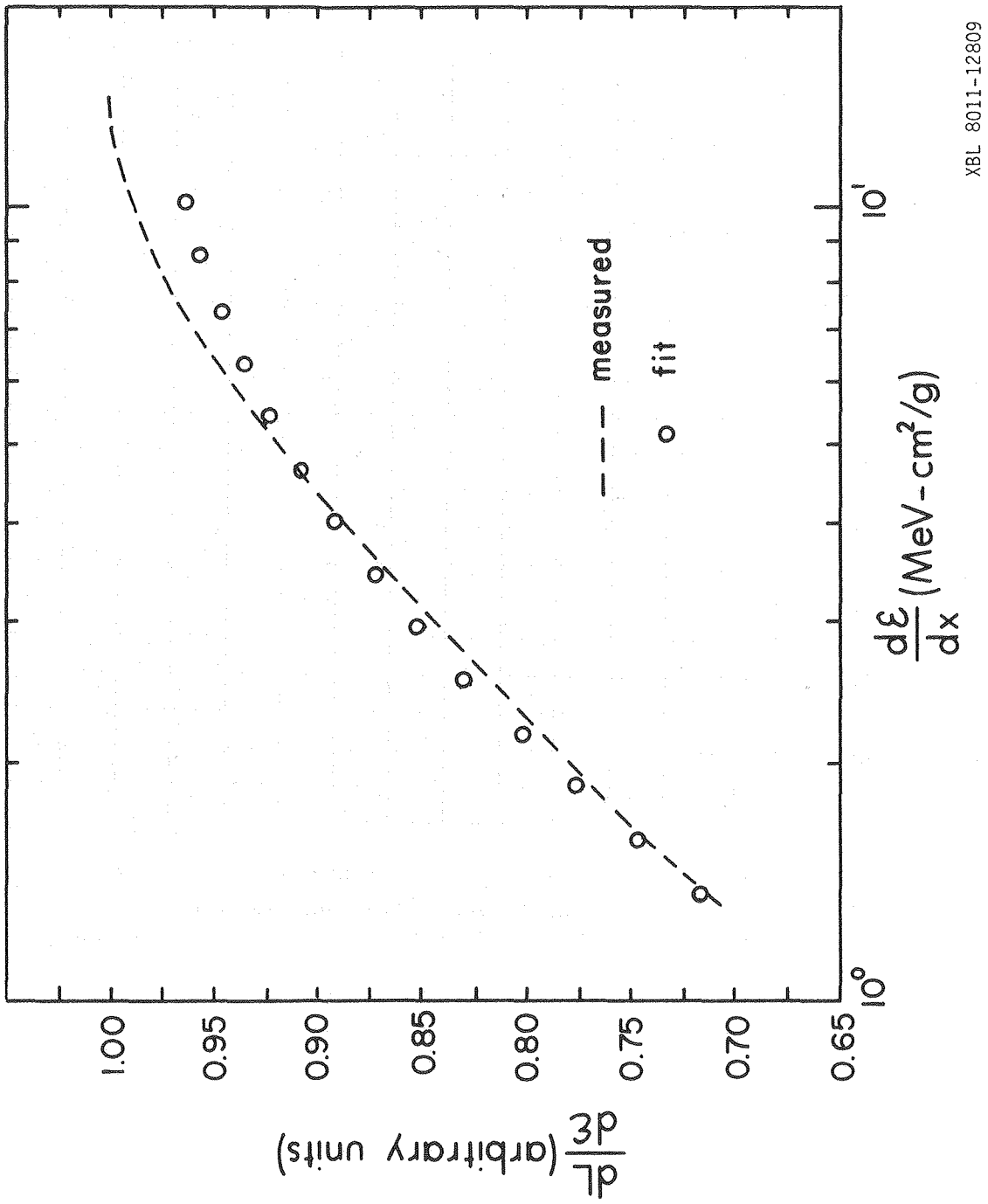
1.00
0.95
0.90
0.85
0.80
0.75
0.70
0.65
$\frac{dL}{d\varepsilon}$ (arbitrary units)
10^0
10^1
$\frac{d\varepsilon}{dx}$ (MeV-cm^2/g)
measured
fit
XBL 8011-12809

Figure 11

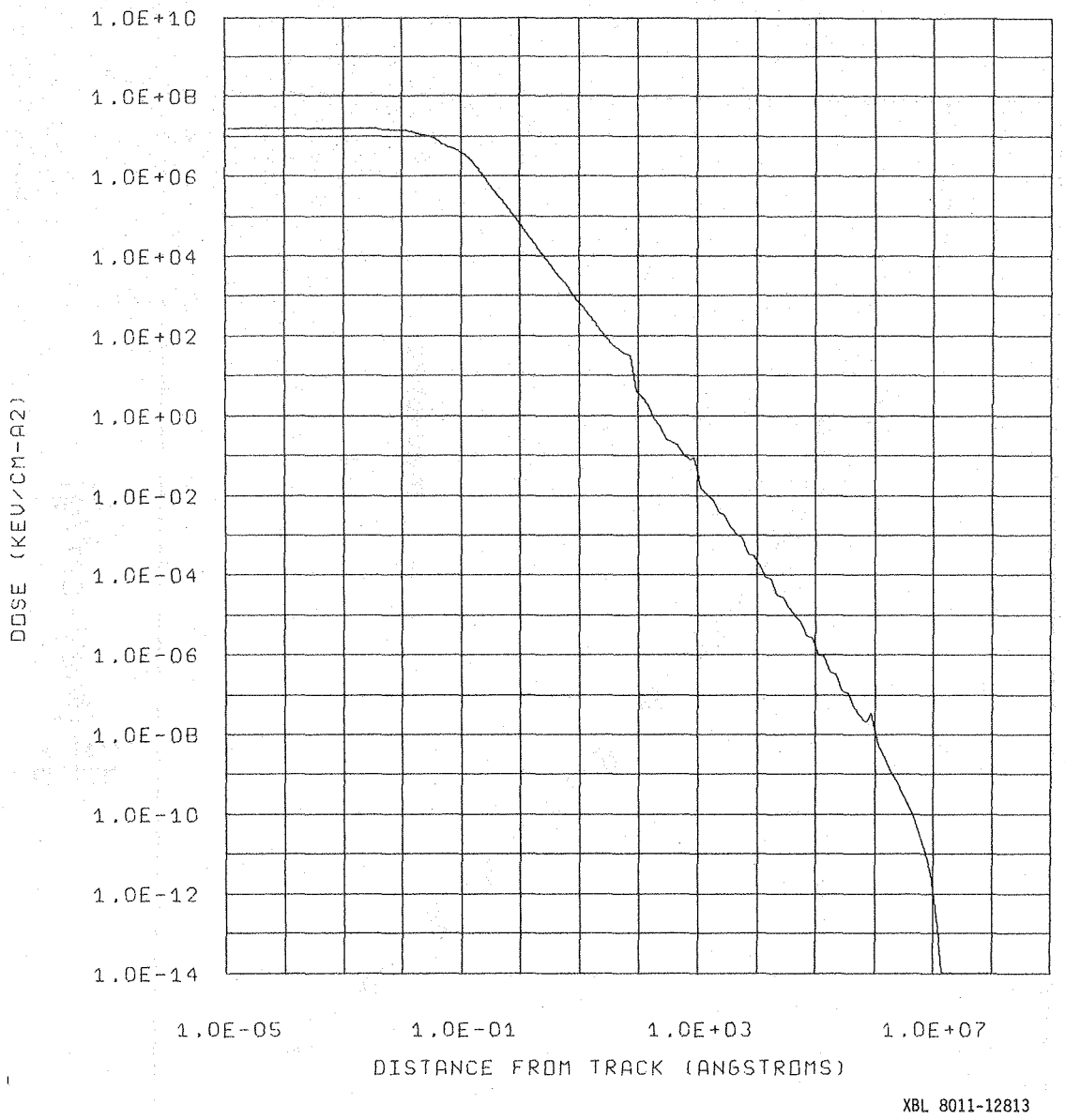
1.0E+10
1.0E+08
1.0E+06
1.0E+04
1.0E+02
1.0E+00
1.0E-02
1.0E-04
1.0E-06
1.0E-08
1.0E-10
1.0E-12
1.0E-14
DOSE (KEV/CM-A2)
1.0E-05
1.0E-01
1.0E+03
1.0E+07
DISTANCE FROM TRACK (ANGSTROMS)
XBL 8011-12813

Figure 12

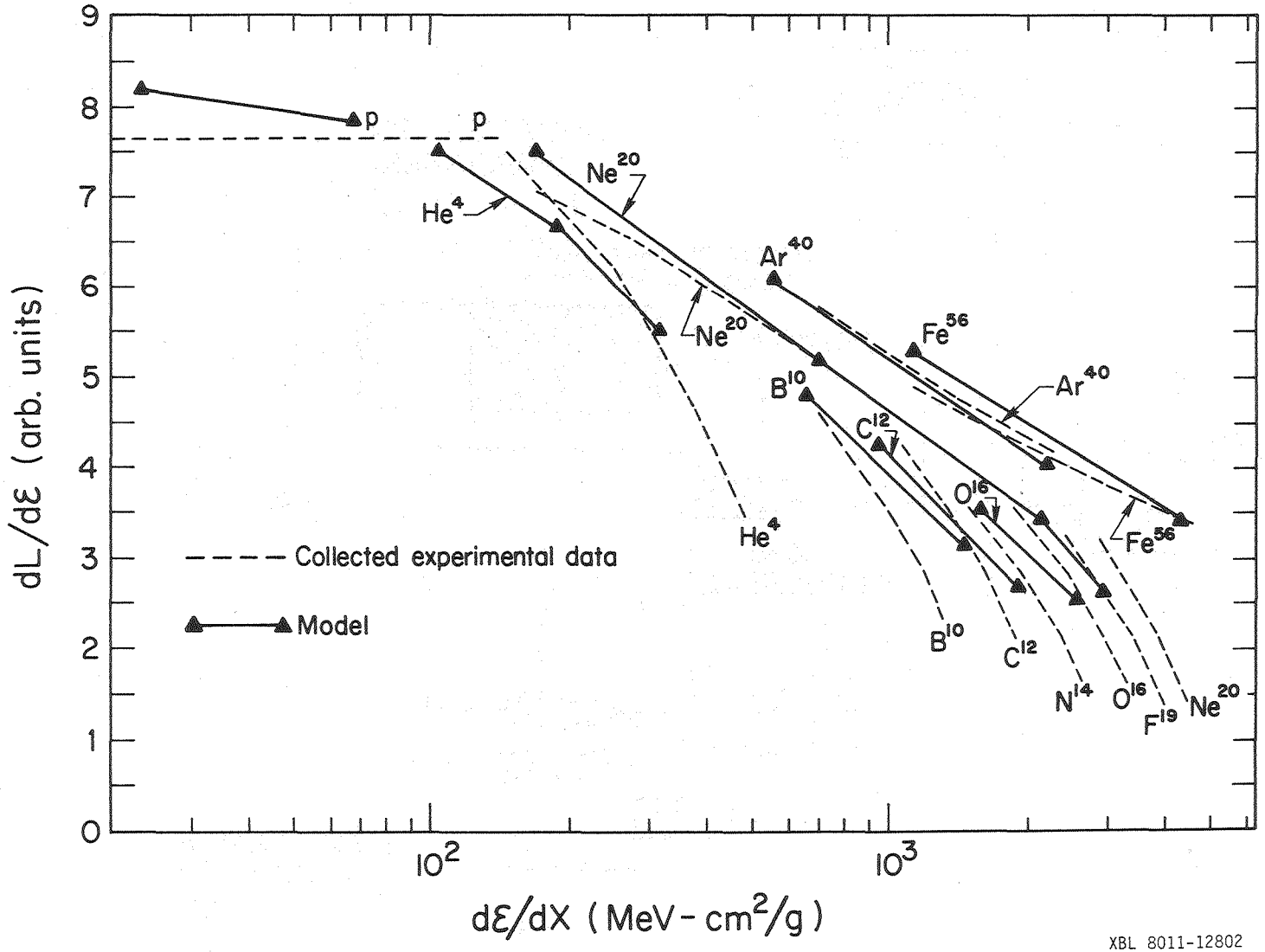
dL/dε (arb. units)
dε/dX (MeV-cm²/g)
Collected experimental data
Model
p
p
He⁴
Ne²⁰
Ne²⁰
Ar⁴⁰
Fe⁵⁶
Ar⁴⁰
B¹⁰
C¹²
O¹⁶
Fe⁵⁶
He⁴
B¹⁰
C¹²
N¹⁴
O¹⁶
F¹⁹
Ne²⁰
XBL 8011-12802

Figure 13

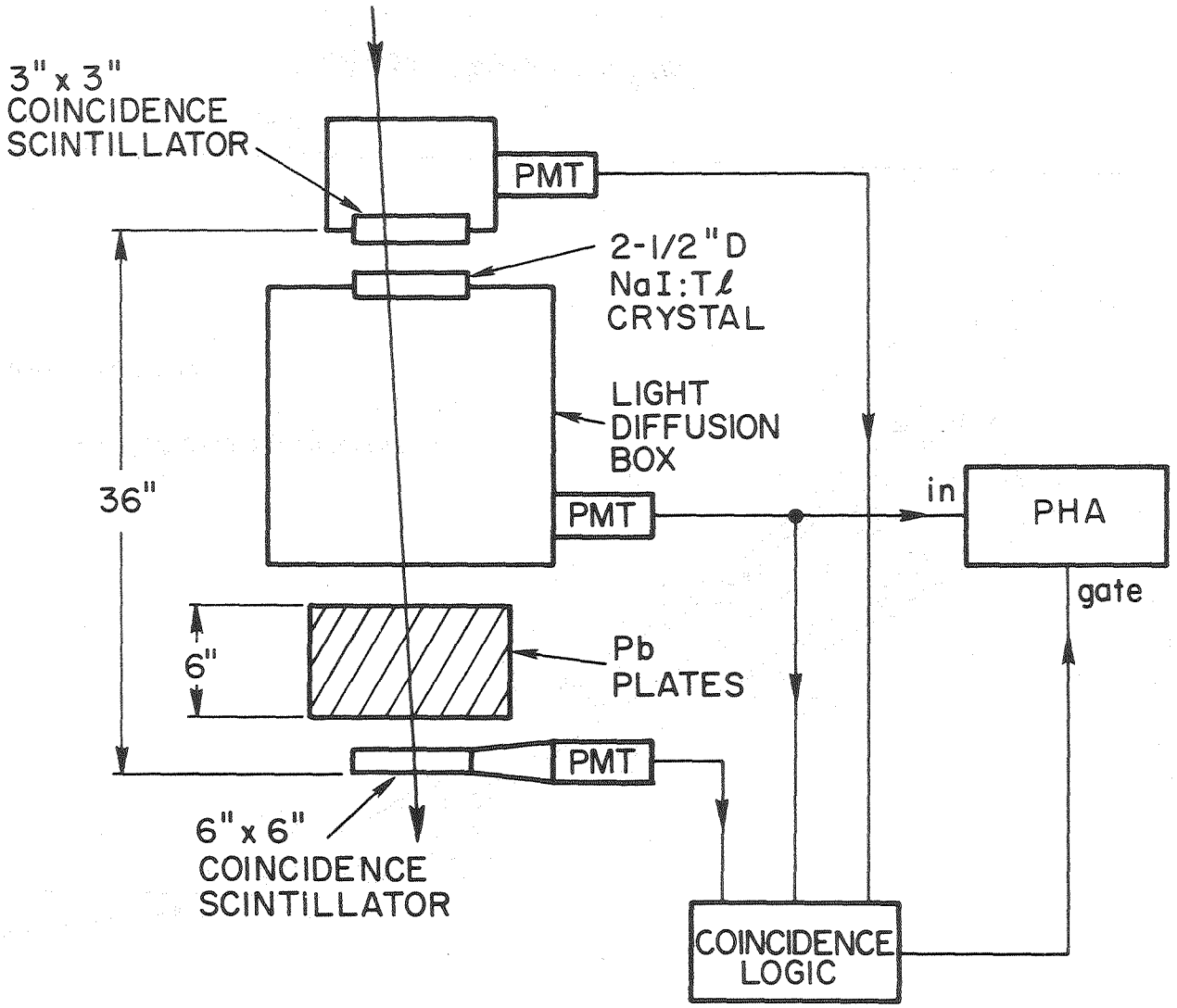
3" x 3"
COINCIDENCE
SCINTILLATOR
PMT
2-1/2" D
NaI:Tℓ
CRYSTAL
LIGHT
DIFFUSION
BOX
36"
PMT
in
PHA
gate
6"
Pb
PLATES
PMT
6" x 6"
COINCIDENCE
SCINTILLATOR
COINCIDENCE
LOGIC
XBL 8011-12807

Figure 14

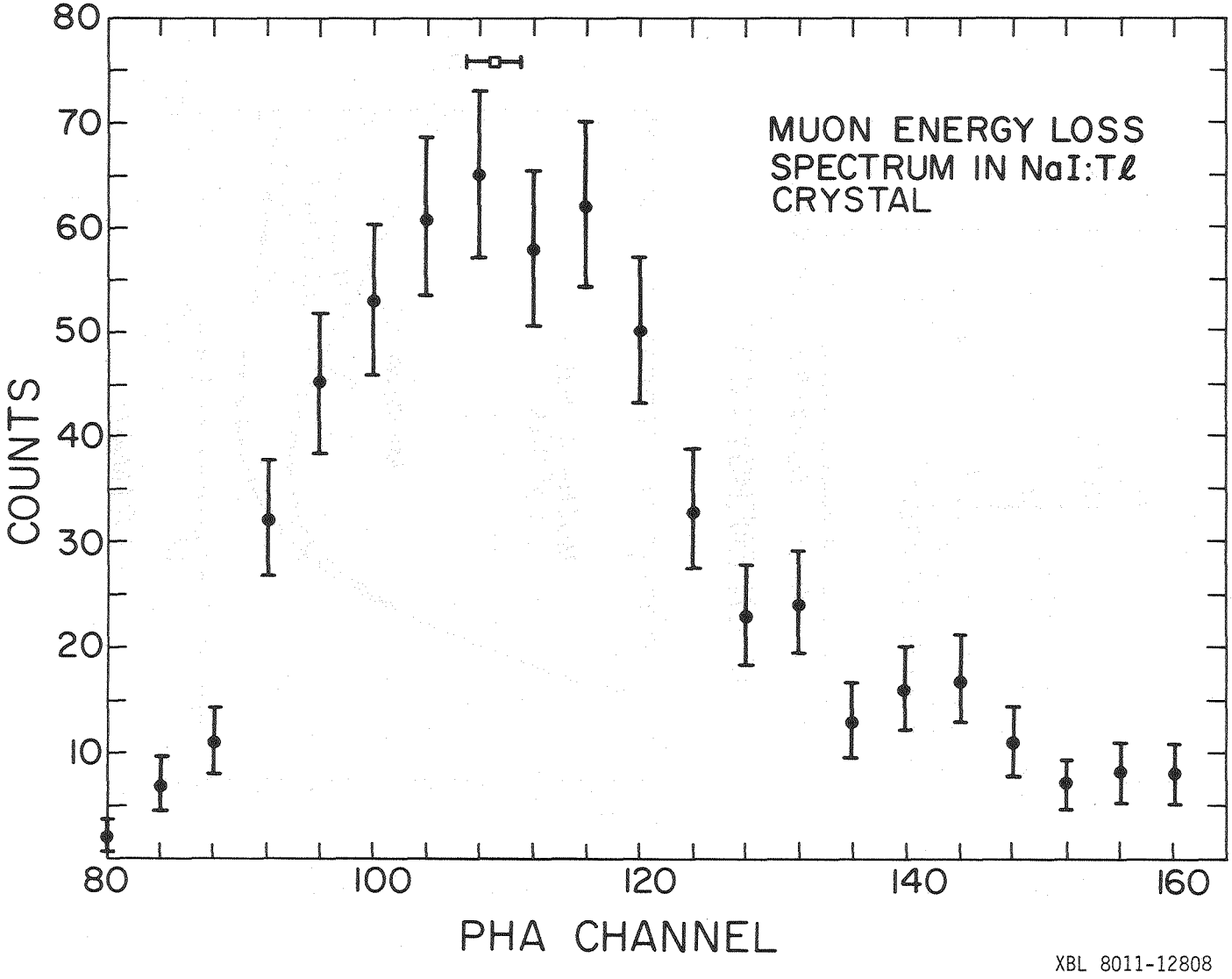
MUON ENERGY LOSS
SPECTRUM IN NaI:Tℓ
CRYSTAL
COUNTS
PHA CHANNEL
80
70
60
50
40
30
20
10
80
100
120
140
160
XBL 8011-12808

Figure 15

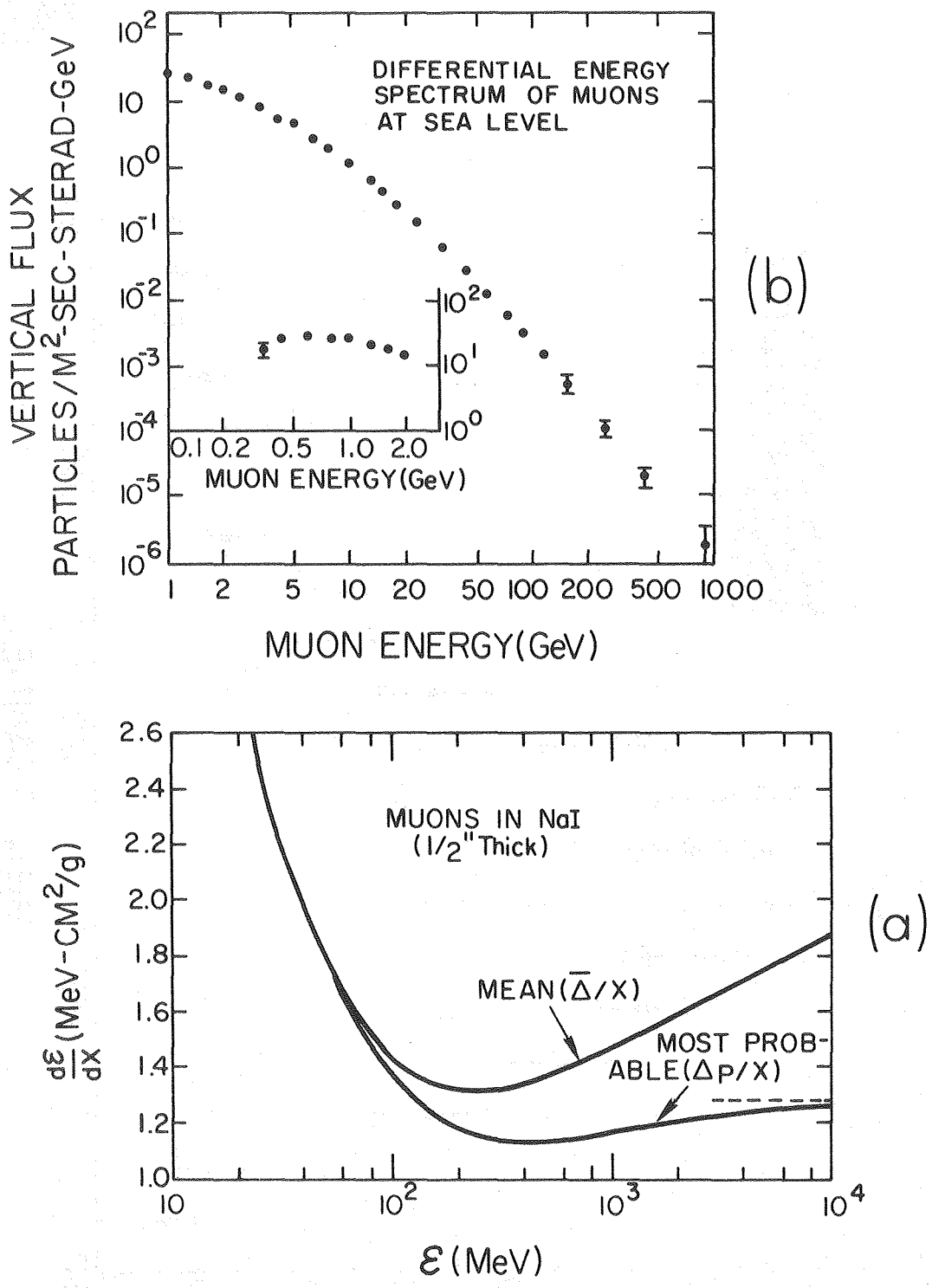
VERTICAL FLUX
PARTICLES/M²-SEC-STERAD-GeV
DIFFERENTIAL ENERGY SPECTRUM OF MUONS AT SEA LEVEL
MUON ENERGY(GeV)
(b)
MUONS IN NaI (1/2" Thick)
MEAN(Δ̄/X)
MOST PROBABLE(ΔP/X)
dε/dX (MeV-CM²/g)
ε (MeV)
(a)
XBL 8011-12803

Figure 16a,b

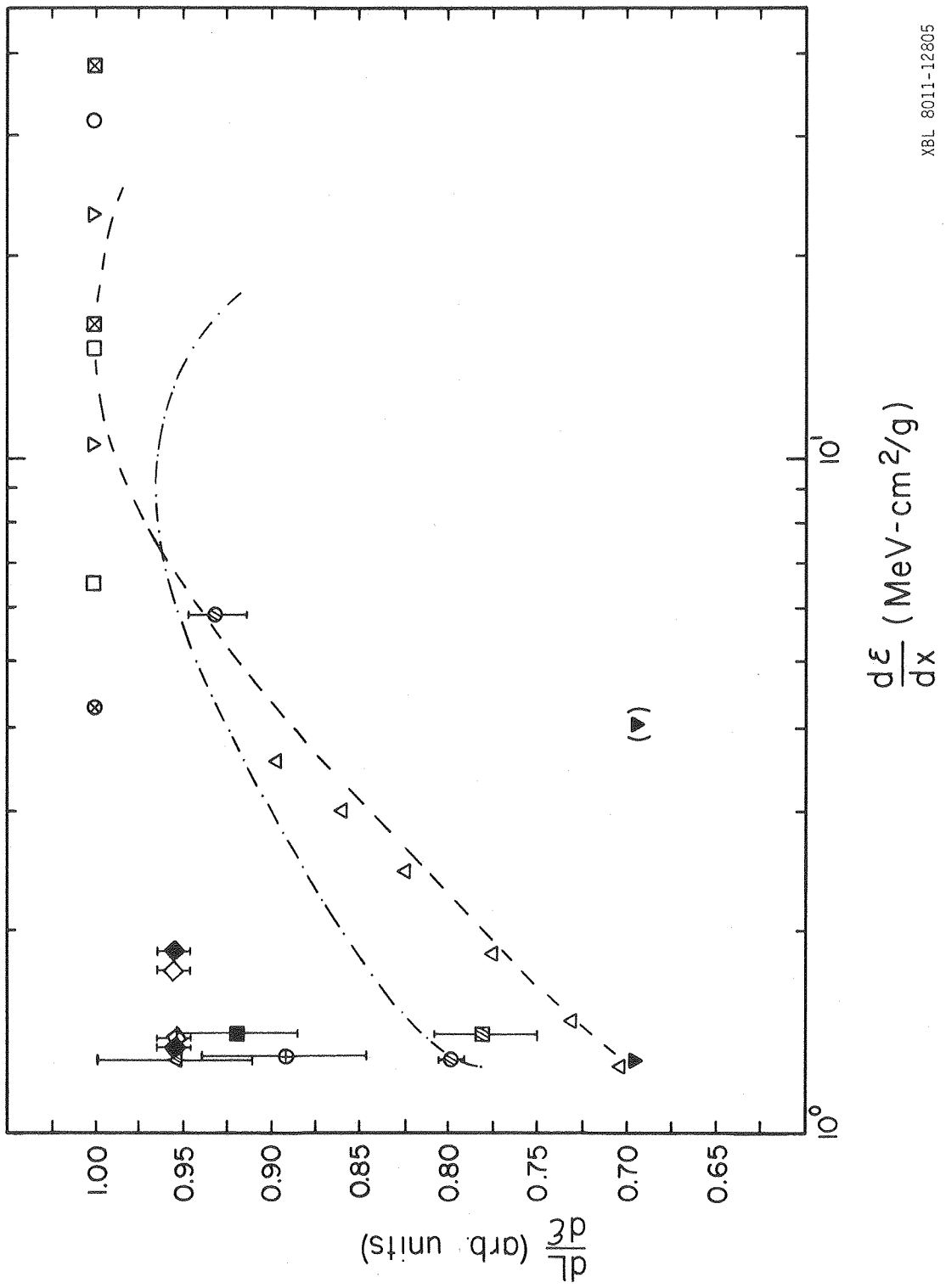
1.00
0.95
0.90
0.85
0.80
0.75
0.70
0.65
$\frac{dL}{d\varepsilon}$ (arb. units)
10^0
10^1
$\frac{d\varepsilon}{dx}$ (MeV-cm^2/g)
XBL 8011-12805

Figure 17